

# 1 An Updated Parameterization of the Unstable Atmospheric Surface 2 Layer in the WRF Modeling System

3 Prabhakar Namdev<sup>1</sup>, Maithili Sharan<sup>1</sup>, Piyush Srivastava<sup>2</sup>, Saroj K. Mishra<sup>1</sup>

4 <sup>1</sup>Centre for Atmospheric Sciences, Indian Institute of Technology Delhi, New Delhi, 110016, India

5 <sup>2</sup>Centre of Excellence in Disaster Mitigation and Management, Indian Institute of Technology Roorkee, Roorkee, 247667,  
6 India

7 *Correspondence to:* Prabhakar Namdev (Prabhakarnmdv587@gmail.com)

8 **Abstract.** Accurate parameterization of atmospheric surface layer processes is crucial for weather forecasts using numerical  
9 weather prediction models. Here, an attempt has been made to improve the surface layer parameterization in the Weather  
10 Research and Forecasting Model (WRFv4.2.2) by implementing similarity functions proposed by Kader and Yaglom (1990)  
11 to make it consistent in producing the transfer coefficient for momentum observed over tropical region (Srivastava and Sharan  
12 2015). The surface layer module in WRFv4.2.2 is modified in such a way that it contains the commonly used similarity  
13 functions for momentum ( $\varphi_m$ ) and heat ( $\varphi_h$ ) under convective conditions instead of the existing single functional form. The  
14 updated module has various alternatives of  $\varphi_m$  and  $\varphi_h$ , which can be controlled by a flag introduced in the input file. The  
15 impacts of utilizing different functional forms have been evaluated using the bulk flux algorithm as well as real-case  
16 simulations with the WRFv4.2.2 model. The model-simulated variables have been evaluated with observational data from a  
17 flux tower at Ranchi (23.412N, 85.440E; India) and the ERA5-Land reanalysis dataset. The transfer coefficient for momentum  
18 simulated using the implemented scheme is found to agree well with its observed non-monotonic behaviour in convective  
19 conditions (Srivastava and Sharan 2022). The study suggests that the updated surface layer scheme performs well in simulating  
20 the surface transfer coefficients and could be potentially utilized for parameterization of surface fluxes under convective  
21 conditions in the WRF model.

## 22 1 Introduction

23 Inadequate representation of near-surface turbulent processes adds significant uncertainty in both climate projections and  
24 seasonal weather forecasts obtained from atmospheric models (Bourassa et al., 2013). Most of the numerical weather prediction  
25 and general circulation models utilize Monin-Obukhov similarity theory (MOST; Monin and Obukhov 1954) to parameterize  
26 surface turbulent fluxes. To estimate these fluxes and near-surface atmospheric variables, the theory utilizes similarity  
27 functions of momentum ( $\varphi_m$ ) and heat ( $\varphi_h$ ) often prescribed as functions of  $\zeta$  (stability parameter). However, the exact  
28 functional forms for these functions have not been provided by MOST, rather it suggests some asymptotic predictions under  
29 near-neutral to very stable and unstable conditions. Over the years, researchers have developed many functional forms for  
30 these functions based on the different experiments, conducted over different locations and have separate expressions for stable

31 and unstable stratifications (Webb, 1970; Businger, 1971; Carl et al., 1973; Dyer, 1974; Hicks, 1976; Holtslag and De Bruin,  
32 1988; Brutsaert, 1992; Bruin, 1999; Wilson, 2001; Cheng & Brutsaert, 2005; Grachev et al., 2007; Gryanik et al. 2020;  
33 Srivastava et al. 2020).

34 In most of the atmospheric models, the commonly used similarity functions under convective conditions are those  
35 proposed by Businger (1966) and A. J. Dyer [1965, unpublished work; see Businger (1988)] and referred to as Businger-Dyer  
36 (BD) functions. However, these functional forms are unable to follow the classical free convection limit. The study by Rao et  
37 al. (1996) suggests that the MOST using Businger relations is unable to define transfer coefficient for momentum ( $C_D$ )  
38 consistent with its observed behaviour, specifically at low wind convective conditions, indicating that MOST needs to be  
39 modified in the (nearly) windless free convection limits. As a result, a revised scaling of heat flux for weakly forced convection  
40 in the atmosphere has been proposed by Rao et al. (2006). Later, the issues of using BD functions in the surface layer scheme  
41 based on the fifth-generation Pennsylvania State University-National Centre for Atmospheric Research Mesoscale Model  
42 (MM5) of a regional scale model (Weather Research and Forecasting; WRF) have been reported in a study by Jimenez et al.  
43 (2012). They implemented the new scheme (referred to as revised MM5 scheme; Jimenez et al., 2012) in the WRF modeling  
44 system and replaced the BD functions by those proposed by Fairall et al. (1996) (F96) under convective conditions. F96  
45 functions are the combination of BD functions and the functions suggested by Carl et al. (1973) and are valid for the entire  
46 range of atmospheric instability. Note that the most recent version of the WRF model still utilizes F96 functions under  
47 convective conditions.

48 Srivastava and Sharan (2015) analyzed the observed behaviour of  $C_D$  over an Indian land surface and suggested that  
49 the observed  $C_D$  shows non-monotonic behaviour with  $-\zeta$ , unlike the behaviour of predicted  $C_D$  from MOST based  
50 parameterization using commonly used  $\varphi_m$  and  $\varphi_h$  (Businger et al., 1971; Carl et al., 1973; Fairall et al., 1996). Later, a  
51 theoretical study by Srivastava and Sharan (2021) revealed that the three-sublayer model based on Kader and Yaglom (1990)  
52 is able to predict  $C_D$  consistent with its observed non-monotonic behaviour. Note that the three-sublayer model has not yet  
53 been newly installed and evaluated in the WRF modeling framework. However, it is already being operational in the surface  
54 layer scheme (Community Land Model; CLM) of National Centre for Atmospheric Research Community Atmosphere Model  
55 version 5 (NCAR-CAM5) as well as Regional Climate Model (RegCM).

56 The study by Srivastava and Sharan (2021) also analyzed the possible uncertainties associated with the use of different  
57 functional forms of  $\varphi_m$  and  $\varphi_h$  under convective conditions. To quantify the impacts of different functional forms, they  
58 classified available  $\varphi_m$  and  $\varphi_h$  in four classes based on the exponents appearing in the expressions of  $\varphi_m$  and  $\varphi_h$  as (1)  
59 functional forms having the exponents of  $\varphi_m$  and  $\varphi_h$  as  $-1/4$  and  $-1/2$ , respectively (Businger et al. 1971; Hogstrom 1996).  
60 (2) functional forms having the exponent of  $\varphi_m$  and  $\varphi_h$  as  $-1/3$  (Carl et al. 1973). (3) functional forms having the exponent  
61 of  $\varphi_m$  and  $\varphi_h$  as  $-1/4$  and  $-1/2$ , respectively in near-neutral conditions while  $-1/3$  in very unstable conditions (Fairall et  
62 al. 1996; Grachev et al. 2000; Fairall et al. 2003). (4) functional forms having the exponent of  $\varphi_m$  and  $\varphi_h$  as  $-1/4$  and  $-1/2$ ,  
63 respectively in near-neutral conditions however,  $1/3$  for  $\varphi_m$  and  $-1/3$  for  $\varphi_h$  in strong unstable conditions (Kader and  
64 Yaglom 1990; Zeng et al. 1998). This study concluded that utilizing different functional forms of similarity functions in the

65 bulk flux algorithm results in a large deviation in the values of estimated fluxes. The detailed description of different functional  
 66 forms for  $\varphi_m$  and  $\varphi_h$  considered in different classes are given in Appendix A. We wish to highlight that all available functional  
 67 forms for  $\varphi_m$  and  $\varphi_h$  under convective conditions fall in one of the classes stated above.

68 The revised MM5 surface layer scheme of the WRF model version 4.2.2 (WRFv4.2.2) employed  $\varphi_m$  and  $\varphi_h$  based  
 69 on Fairall et al. (1996), which belong to class 3. As a result, this scheme is not appropriate in producing  $C_D$  consistent with its  
 70 observed behaviour, specifically over the Indian land as stated above. Recently Namdev et al. (2023) argue that the  
 71 performance of NWP models varies a lot over different seasons and surface types depending upon the functional behaviour of  
 72  $\varphi_m$  and  $\varphi_h$ . Thus, to enhance the potential applicability of the WRF modeling framework, this study attempted to incorporate  
 73 all the commonly used similarity functions under convective conditions along with KY90 as well as existing functional forms  
 74 in the revised MM5 surface layer scheme of WRFv4.2.2. A namelist flag has been introduced in WRF model to choose between  
 75 various  $\varphi_m$  and  $\varphi_h$  in the modified scheme. The modified surface layer scheme proposed in this study has been evaluated  
 76 using offline simulations with bulk flux algorithm as well as the real-case simulations with WRFv4.2.2 during the pre-monsoon  
 77 season (March-April-May) of 2009 over a domain centered around the location of the flux tower installed at Ranchi (23.412N,  
 78 85.440E), India.

## 79 **2 Methodology and data**

### 80 **2.1 Surface flux computation in the WRF modeling system**

81 The Monin-Obukhov similarity theory serves as the foundation for the surface layer parameterization (revised MM5 scheme)  
 82 in the WRF model, and the surface turbulent fluxes are calculated based on the bulk approach using bulk transfer coefficients  
 83 for momentum ( $C_D$ ) and heat ( $C_H$ ) (Namdev et al., 2024; Srivastava et al., 2021; Srivastava and Sharan, 2021). Their  
 84 determination based on MOST using integrated forms of the similarity functions is explained in Appendix B.

85 The transfer coefficients for momentum ( $C_D$ ) and heat ( $C_H$ ) are defined as follows:

$$86 \quad C_D = k^2 \left[ \ln \left( \frac{z + z_0}{z_0} \right) - \left\{ \psi_m \left( \frac{z + z_0}{L} \right) - \psi_m \left( \frac{z_0}{L} \right) \right\} \right]^{-2} \quad (1)$$

$$87 \quad C_H = k^2 \left[ \ln \left( \frac{z + z_0}{z_0} \right) - \left\{ \psi_m \left( \frac{z + z_0}{L} \right) - \psi_m \left( \frac{z_0}{L} \right) \right\} \right]^{-1} \left[ \ln \left( \frac{z + z_h}{z_h} \right) - \left\{ \psi_h \left( \frac{z + z_h}{L} \right) - \psi_h \left( \frac{z_h}{L} \right) \right\} \right]^{-1} \quad (2)$$

88 In which  $k$  is a von Karman constant;  $z_0$  and  $z_h$  are the roughness lengths for momentum and heat, respectively;  $\psi_m$  and  $\psi_h$   
 89 are the integrated similarity functions for momentum and heat, respectively; and  $L$  is the Obukhov length scale.

90 In the following, the default similarity functions used in WRF are explained and other functions are introduced in  
 91 Section 2.2.

92 The default version of the revised MM5 scheme in the WRF model utilizes similarity functions suggested by Cheng  
 93 and Brutsaert (2005) under stable atmospheric conditions ( $\zeta > 0$ ), which are developed using the CASES-99 dataset. The  
 94 integrated forms of functions proposed by Cheng and Brutsaert are

$$95 \quad \psi_m(\zeta) = -a \ln(\zeta + [1 + \zeta^b]^{1/b}), \quad \zeta > 0 \quad (3)$$

$$96 \quad \psi_h(\zeta) = -c \ln(\zeta + [1 + \zeta^d]^{1/d}), \quad \zeta > 0 \quad (4)$$

97 where  $d = 1.1$ ,  $c = 5.3$ ,  $b = 2.5$  and  $d = 6.1$ .

98 On the other hand, the similarity functions for unstable atmospheric surface layer ( $\zeta < 0$ ) are those proposed by  
99 Fairall et al. (1996; F96). The corresponding integrated functional forms  $\psi_m$  and  $\psi_h$  are defined as:

$$100 \quad \psi_\alpha(\zeta) = \frac{\psi_{\alpha BD}(\zeta) + \zeta^2 \psi_{\alpha conv}(\zeta)}{1 + \zeta^2}, \quad \alpha = m, h. \quad (5)$$

101 where  $\psi_{\alpha BD}$  and  $\psi_{\alpha conv}$  denote the integrated functional forms based on Businger and Dyer, and Carl et al. (1973),  
102 respectively. The expressions for  $\psi_{\alpha BD}$  and  $\psi_{\alpha conv}$  are

$$103 \quad \psi_{mBD}(\zeta) = 2 \ln\left(\frac{1+x}{2}\right) + \ln\left(\frac{1+x^2}{2}\right) - 2 \tan^{-1} x + \frac{\pi}{2}, \quad (6)$$

$$104 \quad \psi_{hBD}(\zeta) = 2 \ln\left(\frac{1+x^2}{2}\right), \quad (7)$$

105 in which  $x = (1 - 16\zeta)^{1/4}$  and

$$106 \quad \psi_{\alpha conv} = \frac{3}{2} \ln(y^2 + y + 1/3) - \sqrt{3} \tan^{-1}(2y + 1/\sqrt{3}) + \frac{\pi}{\sqrt{3}} \quad (8)$$

107 with  $y = [1 - \beta_{m,h}\zeta]^{1/3}$ . The values of the constants  $\beta_m$  and  $\beta_h$  are taken as 10 and 34 based on Grachev et al. (2000).

## 108 **2.2 Implementation of different similarity functions**

109 In this section, we briefly describe the implementation of different similarity functions under unstable stratification of surface  
110 layer parameterization of WRFv4.2.2. Note that the functional forms suggested by Carl et al. (1973) and the three sub-layer  
111 model suggested by Kader and Yaglom (1990) for convective conditions have not been included and tested in the revised  
112 MM5 surface layer in the WRF modeling framework.

### 113 **2.2.1 Functions by Businger et al. (1971) (BD71)**

114 Similarity functions suggested by Businger et al. (1971) are based on the KANSAS dataset. These functions do not satisfy the  
115 classical free convection limit as predicted by the MOST. They are already implemented in the old version of the MM5 surface  
116 layer scheme (Grell et al., 1994) in the WRF model. The integrated functional forms ( $\psi_m$  and  $\psi_h$ ) for  $\phi_m$  and  $\phi_h$  stated in

117 Eqns. (A1) and (A2) (Appendix A) are given in Eqns. (6) and (7). BD71 functions have already been used in the old version  
 118 of the MM5 scheme.

### 119 2.2.2 Functions by Carl et al. (1973) (CL73)

120 Carl et al. (1973) proposed an expression of similarity functions  $\varphi_m$  and  $\varphi_h$  valid for the stability range  $-10 \leq \zeta \leq 0$ . The  
 121 expressions for  $\varphi_m$  and  $\varphi_h$  are given in Eqns. (A3) and (A4) (Appendix A). The similarity functions proposed by Carl et al.  
 122 (1973) have not been analyzed in the surface layer scheme of the WRF model. The integrated forms ( $\psi_m$  and  $\psi_h$ ) of similarity  
 123 functions  $\varphi_m$  and  $\varphi_h$  are given by Eqn. (8).

### 124 2.2.3 Functions by Kader and Yaglom (1990) (KY90)

125 Kader and Yaglom (1990) introduced a three-sublayer model for convective conditions. The three sublayers are categorized  
 126 based on  $\zeta$  values as (1) the dynamic sublayer which corresponds to near-neutral conditions, (2) the dynamic convective  
 127 sublayer which corresponds to moderately unstable conditions and (3) the free convective conditions. The present study  
 128 utilized  $\varphi_m$  and  $\varphi_h$  expressions given in Eqns. (A9), and (A10) (Appendix A) that are being used in the surface layer scheme  
 129 (CLM4.0; Zeng et al. 1998) of NCAR-CAM5 model. The corresponding integrated forms for  $\varphi_m$  and  $\varphi_h$  are

$$130 \quad \psi_m(\zeta) = \begin{cases} \psi_{m1}(\zeta_m) + \ln \frac{\zeta}{\zeta_m} - 1.14 [(-\zeta)^{1/3} - (-\zeta_m)^{1/3}], & \zeta \leq -1.574 (= \zeta_m) \\ \psi_{m1}(\zeta) = 2 \ln \left( \frac{1+x}{2} \right) + \ln \left( \frac{1+x^2}{2} \right) - 2 \tan^{-1} x + \frac{\pi}{2}, & -1.574 < \zeta < 0 \end{cases} \quad (9)$$

$$131 \quad \psi_h(\zeta) = \begin{cases} \psi_{h1}(\zeta_h) + \ln \frac{\zeta}{\zeta_h} - 0.8 [(-\zeta)^{-1/3} - (-\zeta_h)^{-1/3}], & \zeta \leq -0.465 (= \zeta_h) \\ \psi_{h1}(\zeta) = 2 \ln \left( \frac{1+x^2}{2} \right), & -0.465 < \zeta < 0 \end{cases} \quad (10)$$

132 where  $x = (1 - 16\zeta)^{1/4}$ .

133 Note that all the functions stated above have been newly installed in the revised MM5 surface layer scheme of  
 134 WRFv4.2.2 and can be used in place of F96 functions already employed in the model. Here, we have introduced a new surface  
 135 layer module where different options for  $\varphi_m$  and  $\varphi_h$  can be controlled using an appropriate value of namelist parameter  
 136 (psimhu\_opt). The parameter psimhu\_opt is added under the physics section of the namelist file. The variable psimhu\_opt can  
 137 have values 0, 1, 2, and 3 for different options for functions F96 (default), BD71, CL73, and KY90, respectively. A brief  
 138 structure and different choices for psimhu\_opt based on newly installed and default functional forms of  $\varphi_m$  and  $\varphi_h$  in the  
 139 default and modified revised MM5 scheme are shown in Figure 1.

### 140 2.3 Characteristics of default and newly installed similarity functions

141 The expressions of  $\varphi_m$  and  $\varphi_h$  for different functional forms utilized in this study are stated in Appendix A. Figure S1  
142 (supplementary material) shows the variation of different (a)  $\varphi_m$  and (b)  $\varphi_h$  under moderately to strongly unstable conditions.  
143 It is evident from Figure S1 that all the different functional forms provide similar values of  $\varphi_m$  and  $\varphi_h$  in near-neutral to  
144 moderately unstable conditions (up to  $\zeta = -0.1$  approximately). However, at higher instabilities one can expect noticeable  
145 differences between different functional forms of  $\varphi_m$  and  $\varphi_h$ . Note that the functional forms for  $\varphi_m$  corresponding to BD71  
146 and CL73 decrease continuously on increasing instability; however,  $\varphi_m$  corresponding to KY90 functional forms show  
147 decreasing behaviour in near-neutral to moderately unstable conditions and attain a minimum at  $\zeta = -1.574$ , and, as the  
148 instability further increases, it starts increasing with  $-\zeta$  (Figure S1a). This implies that  $\varphi_m$  based on class 4 functions shows  
149 non-monotonic behaviour which contradicts the classical MOST prediction. On the other hand, in case of  $\varphi_h$ , all the functional  
150 forms provide continuously decreasing behaviour of  $\varphi_h$  from near-neutral to moderately unstable conditions (Figure S1b).

151 Figure 2 illustrates the variation of default (F96) and newly installed integrated similarity functions  $\psi_m$  and  $\psi_h$   
152 (BD71, CL73, and KY90) with respect to  $-\zeta$ . It is observed from Figure 2a that  $\psi_m$  corresponding to F96, BD71, and CL73  
153 functional forms increases continuously with  $-\zeta$  in moderately to strongly unstable conditions. However, a non-monotonic  
154 behaviour has been observed for  $\psi_m$  corresponding to the KY90 functions implying it first increases with  $-\zeta$  and reaches a  
155 maximum at  $\zeta = -1.574$  and then starts decreasing as instability further grows. On the other hand,  $\psi_h$  corresponding to all  
156 the considered functional forms increases continuously in near-neutral to strong unstable conditions. However, the rate of  
157 increase is slightly higher for F96 in comparison to the other three functions while results of all other functions (BD71, CL73,  
158 and KY90) are very similar to each other (Fig. 2b).

### 159 2.4 Observational data for model evaluation

160 For the evaluation of different simulations corresponding to newly installed similarity functions, observational data derived  
161 from the micrometeorological tower installed at Ranchi (India) has been utilized (Srivastava and Sharan, 2019; Srivastava et  
162 al., 2020; 2021). The dataset (Ranchi data) is derived from an instrument mounted on a 32-m tall tower at the Birla Institute  
163 of Technology Mesra in Ranchi, India (Dwivedi et al., 2014) with an average elevation of 609 m above sea level in a tropical  
164 region. The site has a few buildings in between east and northwest; agriculture land in between northwest and west; and  
165 residential area, and dense trees in between southeast and east. The site also has a relatively flat area in between southeast and  
166 west which is free from any obstacle (Srivastava and Sharan, 2015). A fast response sensor (CSAT3 Sonic Anemometer) at a  
167 height of 10 m with an average elevation 609 m above sea level provides the temperature and the three components of wind at  
168 a 10 Hz frequency. The eddy covariance technique (Stull 1988) is used to estimate heat and momentum fluxes at one-hour  
169 time resolution, however the hourly temperature at 2-m is determined by averaging temperature observations available at a  
170 temporal scale of 1 minute from the slow response sensors located at logarithmic heights on the same tower. We have utilized

171 hourly data for considered variables. The roughness length for momentum ( $z_0$ ) over the Ranchi domain is found to be around  
172 0.016 m based on the study by Reddy and Rao (2016) that utilized the profile method to compute the values of  $z_0$  based on  
173 the observed data from June 2011 to May 2012. However, we have also computed the value of  $z_0$  based on the observational  
174 data utilized in the present study but the value comes out to be higher than that suggested by Reddy and Rao (2016) and needs  
175 to be further validated. Apart from this we have also utilized the ERA5-Land reanalysis dataset available at  $0.10^\circ \times 0.10^\circ$   
176 spatial resolution to evaluate the spatial distribution of the model simulated near surface atmospheric variables. For  
177 consistency, we have regridded the model output to the same grid resolution of reanalysis/observed dataset.

### 178 **3 Numerical simulations**

179 To analyze the impacts of newly installed similarity functions together with the existing functional forms in surface layer  
180 scheme of WRFv4.2.2, the performance of the default and newly installed similarity functions is investigated in two steps. The  
181 first one is independent of the WRF model. Namely, we apply Eqn. (B8) (Appendix B) to iteratively determine  $C_D$  and  $C_H$  as  
182 a function of  $\zeta$  by prescribing the bulk Richardson number ( $Ri_B$ ) and surface roughness parameters for momentum ( $z_0$ ) and  
183 heat ( $z_h$ ). Note that the values of  $z_0$  and  $z_h$  are assumed to be same. The value of  $\zeta$  is estimated by calculating the root of least  
184 magnitude of Eqn. (B8) for a given value of  $Ri_B$ . Once  $\zeta$  is calculated then utilizing it in Eqns. (B9) and (B10), the values of  
185  $C_D$  and  $C_H$  can be estimated. We call this in the following offline simulation. For the computation,  $z$  is taken as 10 m and  $Ri_B$   
186 is in the range  $-2 \leq Ri_B \leq 0$ . The offline simulations are carried out over three different surface types by considering surface  
187 roughness ( $z_0$ ) to be 0.01 m (smooth surface), 0.1 m (transition surface) and 1 m (rough surface) to analyze the impact of  
188 roughness of underlying surface on the simulation of  $\zeta$ ,  $C_D$  and  $C_H$ .

189 The second step is to apply all the parameterizations of the similarity functions in the WRF model version 4.2.2 over  
190 an Indian land site whose output is compared then with the observations during the pre-monsoon (March-April-May; MAM)  
191 season of the year 2009. The simulations have been conducted over a nested domain centred around the location of a  
192 micrometeorological tower installed at Ranchi (23.412°N, 85.44°E), India (Figure 3). Domain d01 ( $6 \times 6$  km) consists of 233  
193 east-west and 210 north-south grid points and domain d02 ( $2 \times 2$  km) consists of 223 east-west and 196 north-south grid  
194 points which covers  $1398 \times 1260$  km<sup>2</sup> and  $446 \times 392$  km<sup>2</sup> spatial area around the centre point, respectively. Each domain  
195 was configured with 50 vertical eta levels from surface to top of the atmosphere. We kept five vertical levels below 100 m  
196 height. Initial and boundary conditions were taken from ERA5 global atmospheric reanalysis dataset at a resolution of  
197  $0.25^\circ \times 0.25^\circ$  and boundary conditions were forced every 6 hours. For land use and land cover (LU/LC) information, we  
198 have used dataset from MODIS (Moderate Resolution Imaging Spectroradiometer; Friedl et al., 2002). Various physical

199 parameterizations utilized in the simulations are listed in Appendix C. In this study, four sets of simulations were carried out,  
200 as given in Table 1.

201 Note that the revised MM5 surface layer scheme has lower limits on the values of  $\mathbf{u}_*$  ( $> 0.001 \text{ m s}^{-1}$ ) and  $\mathbf{U}$  ( $> 0.1$   
202  $\text{m s}^{-1}$ ) that allow nocturnal values of  $\mathbf{u}_*$  at night and control  $\text{Ri}_B$  values to be inordinately high, respectively (Jimenez et al.,  
203 2012). However, the stability parameter  $\zeta$  or  $\text{Ri}_B$  is not restricted in the revised MM5 surface layer scheme, which gives  
204 complete freedom to the WRF model to show its sensitivity to the tested similarity functions (Jimenez et al., 2012). Moreover,  
205 some of the LES studies reported in the literature suggest that the friction velocity cannot be zero when the mean wind drops  
206 to zero; i.e., there should be a minimum friction velocity that is proportional to the  $\mathbf{w}_*$  (Schumann, 1980). For this purpose,  
207 the existing version of the revised MM5 scheme sets  $0.001 \text{ m s}^{-1}$  as the minimum value of  $\mathbf{u}_*$  based on the recommendations  
208 by Jimenez et al. (2012). Thus, to avoid the complexity that arises when mean wind drops to zero, the updated revised MM5  
209 scheme proposed in the present study also utilizes a minimum value of  $\mathbf{u}_*$  ( $> 0.001 \text{ m s}^{-1}$ ) as suggested by Jimenez et al.  
210 (2012) in the existing version of the revised MM5 scheme.

211 The whole simulation period is divided into segments of 4 days with 24 h overlapping time between different  
212 segments to ensure continuity. The model is initialized at 0000 UTC of the first day of each simulation and runs for 96 hours.  
213 In order to avoid the potential spin-up problems at the beginning of the simulation, we discard the first day of each simulation  
214 as spin up time and consider the last three days for the analysis (Jimenez et al., 2010; 2012).

215 For the evaluation of the real-case simulations, different statistical parameters such as mean absolute error (MAE),  
216 root mean square error (RMSE), mean bias (MB), index of agreement (IOA), different measures of correlation coefficient  
217 (CC), mean bias (%) (bias), and standard deviation of the model predicted output normalized by that of the observations are  
218 used. A brief description of the performance indicators for validation utilized in the present study is given in Appendix C.

## 219 **4 Results**

### 220 **4.1 Offline simulations**

221 To analyze the functional dependence of  $\zeta$ ,  $C_D$  and  $C_H$  on the utilized forms of similarity functions, the offline simulations  
222 independent of the WRF model have been conducted utilizing newly installed functions (BD71, CL73, and KY90) together  
223 with F96 functions existing in the default version of the surface layer scheme of the WRF model for three different roughness  
224 lengths for momentum ( $z_0$ ), which are representative of smooth ( $z_0 = 0.01 \text{ m}$ ), transition ( $z_0 = 0.1 \text{ m}$ ), and rough  
225 ( $z_0 = 1.0 \text{ m}$ ) surfaces. Different values of  $z_0$  are chosen to analyze the role of  $z_0$  in the simulation of  $\zeta$ ,  $C_D$  and  $C_H$  from  
226 different similarity functions. The results for  $\zeta$  (a1, a2, and a3) with  $\text{Ri}_B$ ,  $C_D$  (b1, b2, and b3) and  $C_H$  (c1, c2, and c3) with  $\zeta$   
227 across various surface types and sublayers have been analyzed (Figure 4). The different sublayers associated with convective  
228 stratification include dynamic (DNS), dynamic-dynamic convective transition (DNS-DCS), dynamic convective (DCS),



229 dynamic convective-free convective transition (DCS-FCS), and free convective (FCS) (Srivastava and Sharan, 2021). Note  
 230 that the sublayers DNS ( $-0.04 \leq \zeta \leq 0$ ) and DNS-DCS transition ( $-0.12 \leq \zeta < -0.04$ ) are corresponding to weakly to  
 231 moderately unstable conditions, while sublayers DCS ( $-1.20 \leq \zeta < -0.12$ ), DCS-FCS ( $-2.0 \leq \zeta < -1.20$ ), and FCS ( $\zeta <$   
 232  $-2.0$ ) belong to moderately to strongly convective conditions (Srivastava and Sharan, 2015). It is observed that the simulated  
 233 values of  $\zeta$  at smaller values of  $Ri_B$  (i.e., in DNS to DCS) from different forms of similarity functions are found to be almost  
 234 identical to the F96 functional forms (Figure 4a1-3). Moreover, results from BD71, CL73 and F96 functions are even similar  
 235 at higher instabilities (i.e. whole range of  $\zeta$  values) while substantial differences have been observed in the simulated values  
 236 of  $\zeta$  for a given  $Ri_B$  from Exp 3 (Figure 4a1-3). Notably, BD71, CL73, and F96 functional forms predict relatively smaller  
 237 absolute values of  $\zeta$  for a given value of  $Ri_B$ . However, KY90 functions are found to produce a relatively larger magnitude of  
 238  $\zeta$  for a given value of  $Ri_B$ . This behaviour is observed to be consistent for all the values of ratio  $z/z_0$  (Figures 4a1-3)  
 239 representative of smooth, transitional, and rough surfaces. A relatively larger magnitude of  $\zeta$  for a given value of  $Ri_B$  and the  
 240 smaller values of  $\psi_m$  and  $\psi_h$  (Figure 2) in KY90 functional forms implies that the momentum and heat fluxes predicted using  
 241 KY90 functions will be smaller than those anticipated in BD71, CL73, and F96 functional forms.

242 Figure 4b1-3 shows the variation of  $C_D$  with  $\zeta$  estimated using BD71, CL73, KY90, and F96 functional forms over  
 243 different surfaces. Notice that the  $C_D$  values calculated from BD71, CL73, and F96 forms of functions are relatively higher  
 244 than those produced by KY90 functional forms and continue to rise as instability progresses from DCS to FCS. It is important  
 245 to highlight that  $C_D$  estimated using KY90 functions shows a non-monotonic behaviour, which is consistent with the observed  
 246 behaviour of  $C_D$  over the Indian region reported in the literature (Srivastava and Sharan, 2019; 2021). Note that this non-  
 247 monotonic behaviour is consistent for all three cases of different roughness lengths (Figure 4b1-3).

248 On the other hand, across all three surfaces, it is observed that the values of  $C_H$  estimated from all four functional  
 249 forms increase with increasing instability (Figure 4c1-3). While the rate of increase of  $C_H$  in KY90 functions is relatively  
 250 slower. Moreover, BD71, CL73, and F96 functions predict almost similar values over all three types of surfaces. Noticeably,  
 251  $C_H$  estimated using KY90 functions also exhibits non-monotonic behaviour with  $\zeta$  over rough surfaces, which contradicts the  
 252 predictions of the other three functional forms. In addition, it is important to note that  $C_D$  and  $C_H$  predicted by KY90 functional  
 253 forms are found to bound by twice their near-neutral values, while the other functional forms predict continuously increasing  
 254 values of  $C_D$  and  $C_H$  on increasing instability.

255 Hence, it is evident that the BD71, CL73, and F96 functional forms predict values of  $\zeta$ ,  $C_D$ , and  $C_H$  that are almost  
 256 same over all the three different surface types. However, using KY90 functions compared to other commonly used  $\varphi_m$  and  
 257  $\varphi_h$ , one can expect a significant reduction in the estimated values of transfer coefficients in moderately to strongly unstable  
 258 stratification.

259 Note that Figure 4 is used to describe the dependence of estimated  $\zeta$ ,  $C_D$ , and  $C_H$  on different functional forms of  
 260 similarity functions and we have estimated these variables for three different values of momentum roughness length ( $z_0$ ),  
 261 which are representative of smooth ( $z_0 = 0.01$  m), transition ( $z_0 = 0.1$  m), and rough ( $z_0 = 1.0$  m) surfaces. Since the

262 observational data site has a different roughness length for momentum, thus we have not included the observed  $C_D$  in Figure  
263 4.

## 264 4.2 Results of the WRF model using different sets of integrated similarity functions

265 In this section, observational and reanalysis datasets have been used to analyze the simulations performed with WRFv4.2.2  
266 utilizing newly installed and default  $\varphi_m$  and  $\varphi_h$ . The model simulated output has been extracted at the location of flux tower  
267 and compared against the observations derived from the flux tower installed at Ranchi (23.412N, 85.440E), India. The mean  
268 spatial patterns of certain variables averaged over daytime (04:00-12:00 UTC) have been compared against the ERA5-Land  
269 reanalysis dataset. Further, to access the effects of newly installed functions under free convective conditions, the mean spatial  
270 patterns of considered variables averaged across strong convective conditions (hours in which  $\zeta < -10$  over most of the  
271 domain) have been analyzed against respective hours of ERA5-Land reanalysis data. Bilinear interpolation has been used to  
272 interpolate the model output to the same grid resolution as the ERA5-Land data in order to allow a consistent comparison.

### 273 4.2.1 Evaluation against observations derived from flux tower installed at Ranchi (India)

274 Figure 5 depicts the variation of (a)  $\zeta$  with  $Ri_B$ , (b)  $C_D$ , and (c)  $C_H$  with  $\zeta$  from different experiments (Exp1, Exp2, and Exp3)  
275 and CTRL simulation. The variation of simulated  $\zeta$  with  $Ri_B$ ,  $C_D$ , and  $C_H$  with  $\zeta$  is found to be almost identical with offline  
276 results as the  $Ri_B$ - $\zeta$  curves depend only on the height and roughness parameters. The values of simulated variables are found  
277 to be almost identical in DNS to DCS sublayers for all the experiments. Moreover, in FCS, the results obtained from Exp1, 2  
278 and CTRL simulation are found to be nearly similar however, relatively strong differences have been observed in results from  
279 Exp 3 (Figure 5a, b, and c). Simulated  $\zeta$  for a given  $Ri_B$  in Exp2 and CTRL simulation are similar and found to be relatively  
280 smaller in magnitude than Exp1 and Exp3 in FCS. However, the absolute values of  $\zeta$  in Exp3 (KY90 functions) are relatively  
281 higher in FCS than in all other experiments.

282 Figure 5b shows the variation of simulated  $C_D$  with  $\zeta$  from different experiments. Purple circles denote the variation  
283 of observed  $C_D$  with  $\zeta$  at the location of flux tower (Figure 5b). It is found that the observed  $C_D$  increases as the instability  
284 increases from DNS to DCS and has the maximum value in the DCS (at  $\zeta = -0.1$  approx.) and then starts to decrease as  
285 instability grows further from DCS to FCS. It is evident that  $C_D$  simulated using  $\varphi_m$  and  $\varphi_h$  based on class 4 functions (Exp3)  
286 exhibits non-monotonic behaviour (Figure 5b), which is consistent with the observed behaviour of  $C_D$  (Srivastava and Sharan,  
287 2015; 2021). The magnitude of  $C_D$  predicted in Exp3 is significantly smaller than that simulated from other experiments as  
288 well as CTRL simulation, specifically in FCS. This may be due to the large differences between the KY90 functional forms of  
289  $\psi_m$  and  $\psi_h$  and other forms of functions. On the other hand,  $C_D$  simulated using  $\varphi_m$  and  $\varphi_h$  based on the first three classes  
290 (Exp1, Exp2, and CTRL simulation) increases continuously as instability grows from DNS to FCS (Figure 5b).

291 However, it is found that the  $C_D$  predicted from the original forms of class 4 functions (Exp3) show large disagreement  
292 with its observed behaviour, as the predicted  $C_D$  starts decreasing at  $\zeta$  lying in FCS, which is different from that observed, i.e.,  
293  $\zeta$  lying in DCS. As a result, the study also highlighted the necessity of fine-tuning the original KY90 functional forms and  
294 evaluating their performance in the WRF model with additional observational datasets from various land sites and seasons.

295 Note that Srivastava and Sharan (2021) tuned the original forms of class 4 functions by enforcing the matching of the  
296 point at which both observed and model predicted  $C_D$  attain their maximum value. However, more studies in terms of predicting  
297 the observed variation of the non-dimensional vertical gradients of mean wind speed and temperature with  $\zeta$  are essential to  
298 further tune the original KY90 functions for the Indian region using observed data from various locations under different  
299 seasons.

300 Further, we would like to point out that currently no observational datasets are available which show a better  
301 agreement with the KY90 functions over Indian land. However, it is desirable to further validate these functional forms over  
302 Indian land once such observational datasets become available.

303 We wish to highlight that utilizing KY90 (Exp3) functions in the revised MM5 scheme of the WRF model makes it  
304 consistent in predicting  $C_D$  with its observed non-monotonic behaviour over the Indian region.

305 The variation of simulated  $C_H$  with  $\zeta$  from different experiments is shown in Figure 5c.  $C_H$  simulated from Exp1-3 as  
306 well as CTRL simulation shows continuously increasing behaviour with  $\zeta$ . The magnitude of simulated  $C_H$  from CTRL  
307 simulation and Exp1-2 is relatively higher than that of Exp3 in FCS beyond  $\zeta < -10$  (approximately). It is also evident that  
308 at higher instabilities, even  $C_H$  shows non-monotonic behaviour with  $\zeta$  (Figure 5c). We wish to point out that a relatively larger  
309 scatter has been observed in the values of  $C_H$  than  $C_D$ . To the best of our knowledge, the WRF model utilizes constant values  
310 for roughness lengths, with momentum and scalar roughness lengths considered to be similar. However, the relatively large  
311 scatter in the values of  $C_H$  simulated from the WRF model may be linked with the fluctuations in the temperature difference  
312 term  $(\theta_a - \theta_g)$ .

313 The analysis presented here indicates that the KY90 functions in the revised MM5 surface layer scheme are found to  
314 be appropriate in producing non-monotonic behaviour of  $C_D$  consistent with its observed nature. However, all other functional  
315 forms of  $\varphi_m$  and  $\varphi_h$  produce  $C_D$ , which increases continuously with  $\zeta$  from DNS to FCS.

316 To quantify the uncertainties involved in the simulated surface fluxes and certain near-surface variables using KY90  
317 (Exp3) as well as other functional forms (Exp1-2 and CTRL simulation), model simulations have been compared against the  
318 observations. Figure 6 compares the model-simulated (a)  $u_*^2$  ( $\text{m}^2 \text{s}^{-2}$ ) (representative of momentum flux), (b) SHF ( $\text{W m}^{-2}$ )  
319 (sensible heat flux), (c)  $U_{10}$  ( $\text{m s}^{-1}$ ) (10-m wind speed), and (d)  $T_{2m}$  (K) (2-m temperature) with the observed data obtained  
320 from the flux tower at Ranchi (23.412N, 85.440E), India. The model output was extracted at a single grid point closest to the  
321 flux tower to allow a consistent comparison. In Figure 7, a Taylor diagram is displayed along with the normalized standard  
322 deviations and correlations of considered variables. Figure 8 shows the scatter plot between CC vs. RMSE for considered  
323 variables simulated using different experiments. In case of  $u_*^2$ , Exp1 and Exp2 are found to be comparable to the CTRL

324 simulation, while Exp3 considerably improved the simulation of  $u_*^2$  (Figures 6a, 7 and 8). Exp3 reduced MAE (RMSE) from  
325 0.09 (0.16)  $\text{m}^2 \text{s}^{-2}$  to 0.08 (0.14)  $\text{m}^2 \text{s}^{-2}$  (Table 2; Figures 7 and 8) and improved the CC (0.74) and IOA (0.84) for  $u_*^2$  (Table 2).  
326 A Q-Q plot is shown in Figure S2a (supplementary material) suggesting that Exp3 (KY90 functions) is found to be slightly  
327 better than all other experiments and CTRL simulation for  $u_*^2$ . For SHF, all the experiments are comparable to the CTRL  
328 simulation; however, Exp3 shows less scatter than other experiments (Figure 6a).

329 In case of  $U_{10}$ , Exp3 shows less scatter and appears to be closer to the observations than other experiments (Figure  
330 6c). Exp3 noticeably improved the simulation of  $U_{10}$  by reducing MAE (RMSE) from 1.20 (1.54)  $\text{m s}^{-2}$  to 1.16 (1.47)  $\text{m s}^{-2}$  and  
331 MB up to 5 % (Figures 6c, and 7; Table 2). It considerably improved the CC (IOA) for  $U_{10}$  from 0.66 (0.73) to 0.68 (0.75)  
332 (Figure 7 and Table 2). A Q-Q plot (Figure S2b: supplementary material) reveals that Exp3 is observed to be better than all  
333 other experiments and CTRL simulation for  $U_{10}$ . Thus, the KY90 functions in the surface layer scheme of the WRF model  
334 considerably improve the model in simulating  $U_{10}$  (Figures. 6c, 7, 8, and S2b) at the location of the flux tower. Further, in case  
335 of  $T_{2m}$ , Figures 7 and 8 exhibit that all the experiments are found to be comparable with the CTRL simulation.

336 Note that earlier studies, especially the ones done in the GABLS model intercomparison projects, have studied the  
337 impacts of the similarity functions on the modelled profiles and fluxes (though mostly for stable conditions). However, they  
338 learnt that applying different stability functions in the surface and boundary layer parameterizations may trigger unnatural  
339 kinks in the model simulated wind speed and temperature profiles. Here, we have analyzed the profiles of  $U_{10}$  and  $T_{2m}$  simulated  
340 from WRF model using different similarity functions in the surface layer scheme for the occurrence of unnatural kinks in their  
341 values. We observed that the  $U_{10}$  predicted from CTRL simulation, as well as different experiments corresponding to different  
342 similarity functions at certain hours goes higher than that of its observed maximum value (approx.  $8 \text{ m s}^{-1}$ ) (Figure S3:  
343 supplementary material). These relatively higher magnitudes may be linked with some localised weather phenomenon  
344 characterized by rapid changes in weather including strong wind, lightning and thunderstorms and are justifiable. However,  
345 the simulated  $T_{2m}$  from different similarity functions are found to be in line with the observed values across the whole  
346 simulation period (Figure S4: supplementary material). This suggests that the values of  $U_{10}$  and  $T_{2m}$  predicted from WRF  
347 model are found to be in justifiable range and no unnatural kinks have been observed.

#### 348 4.2.2 Evaluation of mean spatial distribution of simulated variables against ERA5-Land reanalysis data during daytime

349 In this section, mean spatial distribution of simulated variables from different experiments as well as CTRL simulation  
350 averaged during daytime (04:00-12:00 UTC) for entire simulation period, is compared with the ERA5-Land reanalysis data.  
351 Figure 9 depicts the mean spatial patterns of simulated  $\zeta$  ( $= \frac{z}{L}$ ) ( $a1 - 4$ ),  $C_D$  ( $c1-c4$ ), and  $C_H$  ( $e1-4$ ) from CTRL simulation  
352 and other experiments, as well as their differences with respect to CTRL simulation. It is observed that the absolute value of  $\zeta$   
353 simulated in Exp3 (KY90 functions) is relatively smaller than CTRL simulation (Figure 9b3) across the whole domain, which  
354 is consistent with Figure 5a and offline simulations presented in Figure 4(a1-3). This could be because the magnitude of KY90

355 functions ( $\varphi_m$  and  $\varphi_h$ ) (Figure S1: supplementary material) is relatively smaller than the functions employed in default scheme  
356 (CTRL simulation).

357 On the other hand, Exp1 also provides slightly smaller absolute values of  $\zeta$  (Figure 9b1), while Exp2 is almost  
358 comparable to the CTRL simulation (Figure 9b2). Model simulated  $C_D$  is found to be relatively smaller in Exp3 than CTRL  
359 simulation (Figure 9d3), while Exp1 and Exp2 provide comparable values of  $C_D$  to CTRL simulation (Figure 9d1-2). In the  
360 case of  $C_H$ , the simulated values from different experiments are observed to be comparable to the CTRL simulation over whole  
361 study domain (Figure 9f1-3). Note that simulated  $C_H$  is found to be comparable in all the experiments while slight differences  
362 have been observed in  $C_D$  in Exp3 than all other experiments which may be related to the fact that only  $\varphi_m$  functions are  
363 involved in the computation of  $C_D$  (Eqn. 1), and the differences between  $\varphi_m$  corresponding to Exp3 are relatively more than  
364  $\varphi_h$ , so are the differences in  $C_D$ . The hatched regions in Figure 9 shows the differences between simulated variables from  
365 different experiments with respect to CTRL simulation are statistically significant at 95% confidence level.

366 The slight differences in  $C_D$  in Exp3 reflected further in the simulated  $u_*^2 \text{ m}^2 \text{ s}^{-2}$  (a measure of momentum flux) (Figure  
367 10b3). A slight reduction has been observed in simulated  $u_*^2$  in Exp3 compared to the CTRL simulation over some parts of the  
368 domain (Figure 10b3), while in Exp1 and Exp2 values are comparable with the CTRL simulation (Figure 10b1-2). In case of  
369 SHF and LHF, the mean spatial distribution from all the experiments is found to be consistent with the ERA5-Land reanalysis  
370 data, and the magnitude of differences between model simulation and ERA5-Land data is comparable for all the experiments  
371 (Table S1; supplementary material).

372 For  $T_{2m}$  (upper panel of Figure 11),  $T_s$  (middle panel of Figure 11), and  $U_{10}$  (lower panel of Figure 11), mean spatial  
373 distribution from different experiments and CTRL simulation agreed well with slightly varying magnitude to the ERA5-Land  
374 reanalysis data. A warm bias up to 2 K (3 K) was observed for  $T_{2m}$  ( $T_s$ ) simulated from different experiments and CTRL  
375 simulation over most of the domain. For  $T_{2m}$ , bias, RMSE, and PCC between different experiments together with CTRL  
376 simulation and ERA5-Land reanalysis data are found to be comparable (Table S1; supplementary material). However, Exp3  
377 slightly improved the PCC from 0.50 to 0.51 for  $T_s$  (Table S1; supplementary material). Further, in the case of  $U_{10}$ , all the  
378 simulations exhibit overprediction over the whole domain (lower panel of Figure 11: b1-4) and Exp3 is observed to be slightly  
379 better than all other experiments as well as CTRL simulation as it reduced bias% (RMSE) from 32.28 (0.54)  $\text{m}^2 \text{ s}^{-2}$  to 32.06  
380 (0.53)  $\text{m}^2 \text{ s}^{-2}$  and improved the PCC from 0.89 to 0.91 (Table S1: supplementary material).

### 381 **4.2.3 Evaluation of newly installed functions during strong unstable conditions with respect to ERA5-Land reanalysis** 382 **data**

383 This section describes the impacts of utilizing different similarity functions ( $\varphi_m$  and  $\varphi_h$ ) on simulated variables during highly  
384 convective regime (i.e.,  $\zeta < -10$ ) with respect to the ERA5-Land reanalysis dataset. Since the functional forms of  $\psi_m$  and  $\psi_h$   
385 are almost identical in near-neutral to moderately unstable conditions, however, in strong unstable conditions, the differences  
386 between different functional forms are more pronounced. Thus, the corresponding differences in the simulated values of

387 considered variables are expected to be more pronounced during highly convective regimes. For this purpose, the model output  
388 has been extracted for those hours in daytime which show  $\zeta$  smaller than  $-10$  over most of the domain and compared with the  
389 respective hours of ERA5-Land reanalysis data.

390 Figure S5 (Supplementary material) depicts the mean spatial distribution of  $\zeta$  (a1-4),  $C_D$  (c1-4), and  $C_H$  (e1-4) as well  
391 as their deviations from CTRL simulation. Notice that the magnitude of differences for all variables ( $\zeta$ ,  $C_D$ , and  $C_H$ ) in this  
392 case are found to be larger than the case of mean spatial patterns averaged during the whole daytime (section 6.2.2). It is  
393 evident from Figure S5b3 (supplementary material) that Exp3 produce large absolute values of  $\zeta$  and smaller values of  $C_D$  and  
394  $C_H$  (Figures S5b3, d3 and f3: supplementary material) than all other experiments and the CTRL simulation. While Exp1 and  
395 Exp2 are found to be comparable to the CTRL simulation for both  $C_D$  and  $C_H$  (Figures S5d1-2 and f1-2).

396 The model simulations for  $T_{2m}$  and  $T_s$  do not capture the spatial patterns well in comparison to ERA5-Land data  
397 (Figures S6a1-5 and S7a1-5: supplementary material). All experiments, as well as the CTRL simulation, exhibit overprediction  
398 across the whole domain (Figures S6b1-4 and S7b1-4). We wish to highlight that the differences between various experiments  
399 and CTRL simulation are seen up to 0.5 K for  $T_{2m}$  (Figure S6c1-3: supplementary material) as well as  $T_s$  (Figure S7c1-3)  
400 which is slightly higher than the case of mean spatial patterns averaged over whole daytime (upper and middle panels of Figure  
401 11). For  $T_{2m}$ , it is evident from Figure S6 (supplementary material) and Table 3 that Exp3 noticeably reduced the bias%  
402 (RMSE) from 0.64 (2.13) K to 0.62 (2.10) K and improved the PCC from 0.43 to 0.46 (approximately 6%). In case of  $T_s$  as  
403 well, Exp3 slightly improved the PCC and reduced the bias% (RMSE) from 1.25 (4.01) K to 1.24 (3.97) K (Table 3 and Figure  
404 12).

405 For  $U_{10}$ , the mean spatial patterns simulated using different experiments agreed well with the ERA5-Land reanalysis  
406 data (Figure S8a1-5: supplementary material) and the magnitude of biases is found to be up to 1 m s<sup>-1</sup>. Exp3 outperformed all  
407 other experiments and the CTRL simulation by lowering the bias% from -4.96 to -0.28 m s<sup>-1</sup> and improved the PCC from 0.34  
408 to 0.36 with comparable RMSE values (Figures S8 and 12; Table 3).

409 The results presented so far suggest that the changes corresponding to different functional forms of similarity  
410 functions in the surface layer parameterization of the WRF model are more pronounced in convective conditions during  
411 daytime hours. For the number of grid points over the study domain that are being affected by the changed similarity functions,  
412 no fixed pattern was observed; however, the changes depend on the considered variable and similarity functions. Furthermore,  
413 we observe that the changes are more pronounced in grids that experience strong instability during the daytime.

## 414 5 Summary and concluding remarks

415 In the present study, the revised MM5 surface layer scheme of the WRFv4.2.2 model has been modified to incorporate  $\varphi_m$   
416 and  $\varphi_h$  suggested by Kader and Yaglom (1990) to make it consistent in producing the transfer coefficient for momentum ( $C_D$ )  
417 in line with its observed behaviour. The revised MM5 scheme is modified in such a way that it contains all commonly used  
418  $\varphi_m$  and  $\varphi_h$  under convective conditions instead of a single functional form. Various alternatives of  $\varphi_m$  and  $\varphi_h$  in the modified

419 scheme can be controlled by a flag (psimhu\_opt) that has been introduced in the physics section of the namelist file. The  
420 impacts of utilizing different functional forms of  $\varphi_m$  and  $\varphi_h$  in the proposed scheme have been evaluated using offline  
421 simulations (with bulk flux algorithm) as well as real-case simulations with WRFv4.2.2 model. The model-simulated surface  
422 turbulent fluxes and certain near-surface variables have been compared with observational data from a flux tower at Ranchi  
423 (23.412N, 85.440E; India), and the spatial patterns have been evaluated with the ERA5-Land reanalysis dataset.

424 Offline simulations indicate that at nearly neutral to moderately unstable conditions,  $\zeta$  simulated using various  
425 functional forms of  $\varphi_m$  and  $\varphi_h$  is comparable, and as the instability grows (free convective conditions), the differences  
426 between different experiments become more pronounced. This might be connected to the corresponding variations between  
427 different functional forms of similarity functions in the respective regimes. Similarly, for simulated  $C_D$ , Exp3 (KY90 functions)  
428 demonstrates nonmonotonic behaviour with  $-\zeta$  across all three surface types (representing smooth, transition, and rough  
429 surfaces), which is consistent with its observed behaviour. However, all other experiments and CTRL simulation indicate  
430 continuously increasing  $C_D$  with  $-\zeta$  from near-neutral to free convective conditions over all three surface types, which is  
431 inconsistent with its observed behaviour over the study domain. The non-monotonic behaviour of  $C_D$  in Exp3 (KY90 functions)  
432 may be associated to the analogous non-monotonic behaviour of the corresponding  $\psi_m$  in the respective regime.

433 In real-case simulations, the model simulated  $\zeta$ ,  $C_D$  and  $C_H$  are found to be consistent with the offline simulations.  
434 The variation of  $C_D$  in Exp3 (KY90 functions) with  $-\zeta$  is observed to be nonmonotonic, as reported in offline simulations and  
435 found to be consistent with its observed behaviour. This indicates that the KY90 functions in the surface layer scheme of the  
436 WRF model make it compatible in producing  $C_D$  consistent with its observed behaviour over Indian land. As compared with  
437 the observations over Ranchi (India), the simulations using KY90 (Exp3) functions are found to perform better for most of the  
438 considered variables compared to all other experiments. Further, in the mean spatial distribution averaged during daytime  
439 (04:00–12:00 UTC) over the entire simulation period, the significant increase in absolute value of  $\zeta$  from Exp3 resulted in a  
440 noticeable reduction in the values of  $C_D$  and  $C_H$ , which further impacted the simulated values of  $T_s$ ,  $T_{2m}$ , and  $U_{10}$ . When  
441 compared with the ERA5-Land reanalysis data, the spatial patterns for  $T_{2m}$ ,  $T_s$ , and  $U_{10}$  from Exp3 (KY90 functions) provided  
442 more consistent results. A reduction has been observed in bias (%) and RMSE values for  $T_s$ , and  $U_{10}$ . Moreover, in case of  
443 highly convective regime ( $\zeta < -10$ ), Exp3 (KY90 functions) slightly improved the performance of the model by reducing the  
444 bias (%) and RMSE for  $T_{2m}$ ,  $T_s$ , and  $U_{10}$  and increasing the correlation to some extent.

445 Thus, it is concluded that the similarity functions proposed by Kader and Yaglom (1990) (KY90 functions; Exp3) are  
446 found to be more appropriate for use in the WRF model as they can simulate  $C_D$  consistent with its observed behaviour and  
447 improve simulation for most of the considered variables over the study domain. However, due to the limited spatial coverage  
448 of the domain considered in this study and the limited availability of observational data, KY90 functional forms need to be  
449 further evaluated in the WRF modeling framework utilizing observations from other sites. The modified surface layer scheme  
450 proposed in this study could enhance the potential applicability of the WRF modeling framework for the community in  
451 investigating the role of different functional forms of similarity functions under convective conditions for selected events/case  
452 studies such as extreme weather events, heat waves during summer, cyclonic storms, and fog predictions using the WRF model.

453 **Appendix A**

454 Here, the detailed description of commonly used functions ( $\varphi_m$  and  $\varphi_h$ ) in numerical models under convective conditions is  
 455 provided.

456 Based on Businger (1966) and A. J. Dyer [1965, unpublished work; see Businger (1988) for details] the expressions  
 457 for  $\varphi_m$  and  $\varphi_h$  are as follows:

$$458 \quad \varphi_m = (1 - \gamma_m \zeta)^{-\frac{1}{4}} \quad (A1)$$

$$459 \quad \varphi_h = Pr_t (1 - \gamma_h \zeta)^{-\frac{1}{2}} \quad (A2)$$

460 in which  $\gamma_m = 15$ ,  $\gamma_h = 9$ , and  $Pr_t = 0.74$  is the turbulent Prandtl number. Note that in case of Dyer (1974) the values of  
 461  $\gamma_m = \gamma_h = 16$  and  $Pr_t = 1.0$ . These functions commonly known as Businger-Dyer similarity (BD) functions and do not  
 462 satisfy the classical free convection limit (Srivastava et al. 2021).

463 The similarity functions proposed by Carl et al. (1973) under convective conditions are applicable for the range  
 464  $-10 \leq \zeta \leq 0$ . The expressions for  $\varphi_m$  and  $\varphi_h$  suggested by Carl et al. (1973) are:

$$465 \quad \varphi_m = (1 - \beta_m \zeta)^{-\frac{1}{3}} \quad (A3)$$

$$466 \quad \varphi_h = (1 - \beta_h \zeta)^{-\frac{1}{3}} \quad (A4)$$

467 in which  $\beta_m = \beta_h = 15$ . However, based on various studies reported in the literature  $\beta_m$  and  $\beta_h$  can take different values. For  
 468 example, Delage and Girard (1992) proposed  $\beta_m = \beta_h = 40$ , on the other hand, Fairall et al. (1996) suggested that  $\beta_m = \beta_h =$   
 469 12.87.

470 Fairall et al. (1996, 2003) proposed an interpolation function applicable for the entire range of atmospheric instability,  
 471 which was based on BD functions and functions suggested by Carl et al. (1973). This interpolation function does not have the  
 472 gradient form ( $\varphi_m$  and  $\varphi_h$ ), as they have interpolated the integrated forms of the functions. We wish to highlight that the  
 473 revised MM5 surface layer scheme of Weather Research and Forecasting Model version 4.2.2 utilized the interpolation  
 474 functions suggested by Fairall et al. (1996).

475 Kader and Yaglom (1990) proposed a three-sublayer model under convective conditions. The dynamic sublayer  
 476 corresponds to near-neutral conditions in which  $\varphi_m = 1$  and  $\varphi_h = Pr_t$ . Further, in the dynamic convective sublayer,  
 477 mechanical energy is in the x direction, while buoyancy-induced energy is in the z direction. Thus, in this sublayer, the  
 478 functional forms for similarity functions, as determined by dimensional analysis, are

$$479 \quad \varphi_m(\zeta) = A_u (-\zeta)^{-\frac{1}{3}} \quad (A5)$$

$$480 \quad \varphi_h(\zeta) = A_T (-\zeta)^{-\frac{1}{3}} \quad (A6)$$

481 in which  $A_u$  and  $A_T$  are constants.



482 Moreover, in the free-convective sublayer, buoyancy dominates the mechanical production of energy, and the  
 483 pressure redistribution term feeds the buoyant energy in the vertical direction into the horizontal direction (Kader and Yaglom,  
 484 1990). Thus, in this case, the dimensional analysis suggests

$$485 \quad \varphi_m(\zeta) = B_u(-\zeta)^{\frac{1}{3}} \quad (A7)$$

$$486 \quad \varphi_h(\zeta) = B_T(-\zeta)^{-\frac{1}{3}} \quad (A8)$$

487 in which  $B_u$  and  $B_T$  are constants.

488 Thus, under unstable conditions,  $\varphi_m$  exhibits a nonmonotonic behaviour with respect to  $-\zeta$  as the three sublayer  
 489 theory suggested that for sufficiently large values of  $-\zeta$ ,  $\varphi_m$  varies as the  $+1/3$  power of  $\zeta$ , in contrast to the case of the free  
 490 convection limit, where both  $\varphi_m$  and  $\varphi_h$  follow the  $-1/3$  power law. In the literature, various expressions for  $\varphi_m$  and  $\varphi_h$  are  
 491 available based on the Kader and Yaglom (1990) three-sublayer model. However, the present study employs  $\varphi_m$  and  $\varphi_h$  based  
 492 on the expressions implemented in the surface layer scheme (CLM4.0) of NCAR-CAM5 (Zeng et al., 1998) model. The  
 493 expressions for  $\varphi_m$  and  $\varphi_h$  utilized in this study are as follows:

$$494 \quad \varphi_m = \begin{cases} (1 - 16\zeta)^{-\frac{1}{4}}, & -1.574 \leq \zeta \leq 0 \\ 0.7k^{\frac{2}{3}}(-\zeta)^{\frac{1}{3}}, & \zeta \leq -1.574 \end{cases} \quad (A9)$$

495 and

$$496 \quad \varphi_h = \begin{cases} (1 - 16\zeta)^{-\frac{1}{2}}, & -0.465 \leq \zeta \leq 0 \\ 0.9k^{\frac{4}{3}}(-\zeta)^{-\frac{1}{3}}, & \zeta \leq -0.465 \end{cases} \quad (A10)$$

497

498 Srivastava and Sharan (2021) classified these commonly used similarity functions stated above into four different classes based  
 499 on the exponents appearing in the expressions of  $\varphi_m$  and  $\varphi_h$ . The classification is as follows:

500

501 **Class 1.** This class consists of functions having the exponents of  $\varphi_m$  and  $\varphi_h$  as  $-1/4$  and  $-1/2$  (as in Eqns. A1 and A2),  
 502 respectively from near-neutral to strong unstable conditions.  $\varphi_m$  and  $\varphi_h$  proposed by Businger (1971) and Hogstrom (1996)  
 503 are the examples of class 1 functions.

504

505 **Class 2.** In this class, the similarity functions ( $\varphi_m$  and  $\varphi_h$ ) having exponents of  $\varphi_m$  and  $\varphi_h$  as  $-1/3$  for the entire range from  
 506 near-neutral to moderately unstable conditions (as in Eqns. A3 and A4), respectively are included. The functional forms  
 507 suggested by Carl et al. (1973) are the example of class 2 functions.

508

509 **Class 3.**  $\varphi_m$  and  $\varphi_h$  having exponents as  $-1/4$  and  $-1/2$ , respectively in near-neutral conditions while  $-1/3$  in strong  
 510 unstable conditions are included in this class.  $\varphi_m$  and  $\varphi_h$  based on Fairall et al. (1996), Grachev et al. (2000) and Fairall et al.  
 511 2003 are some examples of class 3 functions.

512

513 **Class 4.** Functional forms of  $\varphi_m$  and  $\varphi_h$  having the exponents as  $-1/4$  and  $-1/2$ , respectively in near-neutral conditions  
 514 however,  $1/3$  for  $\varphi_m$  and  $-1/3$  for  $\varphi_h$  in strong unstable conditions are classified in this class (as in Eqns. A9 and A10). The  
 515 three-sublayer model for  $\varphi_m$  and  $\varphi_h$  suggested by Kader and Yaglom (1990) (Zeng et al. 1998) is one of the examples of  
 516 functions in this class.

## 517 Appendix B

518 This section consists of a brief description of the computation of surface turbulent fluxes in the revised MM5 surface layer  
 519 scheme. In a homogeneous surface layer, the dimensionless wind and temperature gradients are defined as

$$520 \frac{kz \partial U}{u_* \partial z} = \varphi_m(\zeta), \quad (B1)$$

$$521 \frac{kz \partial \theta}{\theta_* \partial z} = \varphi_h(\zeta). \quad (B2)$$

522 where  $L$  denotes the Obukhov length scale and  $U$  is the wind speed at height  $z$ ;  $k$  represents the von Karman constant and its  
 523 value is taken as 0.4. Integrating Eqns. (B1) and (B2) with respect to  $z$  leads to

$$524 U = \frac{u_*}{k} \left[ \ln \left( \frac{z}{z_0} \right) - \left\{ \Psi_m(\zeta) - \Psi_m \left( \frac{z_0}{L} \right) \right\} \right], \quad (B3)$$

$$525 (\theta_a - \theta_g) = \frac{\theta_*}{k} \left[ \ln \left( \frac{z}{z_h} \right) - \left\{ \Psi_h(\zeta) - \Psi_h \left( \frac{z_h}{L} \right) \right\} \right] \quad (B4)$$

526 in which  $\Psi_m$  and  $\Psi_h$  denote the integrated form of similarity functions  $\varphi_m$  and  $\varphi_h$ . The roughness lengths for momentum and  
 527 heat are denoted by  $z_0$  and  $z_h$ , respectively. The ground and surface air potential temperature are denoted by  $\theta_g$  and  $\theta_a$ ,  
 528 respectively.  $\zeta (= \frac{z}{L})$  is the stability parameter and is defined as

$$529 \zeta = \frac{kgz \theta_*}{\theta_a u_*^2} \quad (B5)$$

530  $\Psi_m$  and  $\Psi_h$  can be calculated from the following expression (e.g., Panofsky, 1963):

$$531 \Psi_m(\zeta) = \Psi_h(\zeta) = \int_0^\zeta \frac{1 - \varphi_{m,h,q}(\zeta')}{\zeta'} d\zeta' \quad (B6)$$

532 The bulk Richardson number ( $Ri_B$ ) is given by:

$$533 Ri_B = \frac{g(\theta_a - \theta_g)(z - z_0)^2}{\theta U^2(z - z_h)} \quad (B7)$$

534 Substituting the values of  $U$  and  $(\theta_a - \theta_g)$  from Eqns. (B3) and (B4) in Eqn. (B7), one gets

$$535 Ri_B = \zeta \frac{\left[ \left( 1 - \frac{z_0}{z} \right)^2 \right] \left[ \ln \left( \frac{z}{z_h} \right) - \left\{ \Psi_h(\zeta) - \Psi_h \left( \zeta \frac{z_h}{z} \right) \right\} \right]}{\left[ \left( 1 - \frac{z_h}{z} \right) \right] \left[ \ln \left( \frac{z}{z_0} \right) - \left\{ \Psi_m(\zeta) - \Psi_m \left( \zeta \frac{z_0}{z} \right) \right\} \right]^2} \quad (B8)$$

536 Note that Eqn. (B8) is a transcendental equation, and for a given value of  $Ri_B$ , the corresponding  $\zeta$  value can be calculated  
 537 using any iterative method.

538 The bulk transfer coefficient for momentum ( $C_D$ ) and heat ( $C_H$ ) are defined as:

$$539 \quad C_D = k^2 \left[ \ln \left( \frac{z + z_0}{z_0} \right) - \left\{ \psi_m \left( \frac{z + z_0}{L} \right) - \psi_m \left( \frac{z_0}{L} \right) \right\} \right]^{-2} \quad (B9)$$

$$540 \quad C_H = k^2 \left[ \ln \left( \frac{z + z_0}{z_0} \right) - \left\{ \psi_m \left( \frac{z + z_0}{L} \right) - \psi_m \left( \frac{z_0}{L} \right) \right\} \right]^{-1} \left[ \ln \left( \frac{z + z_h}{z_h} \right) - \left\{ \psi_h \left( \frac{z + z_h}{L} \right) - \psi_h \left( \frac{z_h}{L} \right) \right\} \right]^{-1} \quad (B10)$$

541 Once we get  $C_D$  and  $C_H$ , then the momentum ( $\tau$ ), and sensible heat ( $H$ ) fluxes are calculated using the following expressions:

$$542 \quad \tau = \rho C_D U^2 \quad (B11)$$

$$543 \quad H = -\rho c_p C_H U (\theta_a - \theta_g), \quad (B12)$$

## 544 Appendix C

545 In this section, the details of various physical parameterizations utilized in the real-case simulations using WRFv4.2.2 model  
 546 and the different statistical indicators used for model evaluation.

547 The real-case simulations with the WRFv4.2.2 model utilised the Purdue Lin microphysics scheme (Lin et al., 1983);  
 548 YSU (Hong, Noh, and Dudhia, 2006) PBL scheme; Kain-Fritsch (Kain and John, 2004) cumulus scheme; Dudhia (Dudhia,  
 549 1989) shortwave scheme; RRTM (Mlawer et al., 1997) longwave scheme; Noah-MP land surface model (Niu et al., 2011);  
 550 and revised MM5 surface layer scheme (Jimenez et al., 2012).

551 In the present study, different statistical indicators have been used for the model evaluation with respect to  
 552 observations/reanalysis datasets. Statistical parameters such as mean absolute error (MAE), root mean square error (RMSE),  
 553 mean bias (MB), index of agreement (IOA), and correlation coefficient (CC) are defined as:

554 1. Mean absolute error:

$$555 \quad MAE = \frac{\sum_{i=1}^n |p_i - o_i|}{n}$$

556 2. Root mean square error:

$$557 \quad RMSE = \sqrt{\frac{\sum_{i=1}^n (p_i - o_i)^2}{n}}$$

558 3. Mean bias

$$559 \quad MB = \overline{(p_i - o_i)}$$

560 4. Index of agreement

$$561 \quad IOA = 1 - \frac{\sum_{i=1}^n (o_i - p_i)^2}{\sum_{i=1}^n (|p_i - \bar{o}| + |o_i - \bar{o}|)^2}$$

562 5. Correlation coefficient

$$CC = \frac{\sum_{i=1}^n (p_i - \bar{p})(o_i - \bar{o})}{\sqrt{\sum_{i=1}^n (p_i - \bar{p})^2} \sqrt{\sum_{i=1}^n (o_i - \bar{o})^2}}$$

in which  $p_i$  and  $o_i$  represent the predicted and observed time series, respectively, while  $\bar{p}$  and  $\bar{o}$  are the predicted and observed mean for a considered variable, respectively.

6. Taylor diagram: It exhibits how well patterns match each other in terms of their correlation, ratio of their variances, and root mean square differences (Taylor, 2001).
7. Q-Q plot: It is a graphical technique used to compare the overall distribution of predicted and observed values for a variable (Venkatram, 1999)

The error or deviation between observed and simulated values is measured by MAE, RMSE, and MB. On the other hand, IOA is used to assess the trend relationship, or how closely the magnitudes and signs of the observed values are related to the projected values (Schlunzen and Sokhi 2008). In order to evaluate the spatial patterns with ERA5-Land reanalysis dataset, statistical metrics such as mean bias (%), RMSE, and pattern correlation (PCC) have been used.

**Code and data availability:** Weather Research and Forecasting Model version 4.2.2 (WRFv4.2.2) is an open source model and can be downloaded from [https://www2.mmm.ucar.edu/wrf/users/download/get\\_source.html](https://www2.mmm.ucar.edu/wrf/users/download/get_source.html). The model output at the location of the flux tower at Ranchi (23.412N, 85.440E), India is openly available at <https://doi.org/10.5281/zenodo.10435513>. The raw observational data derived from the flux tower at Ranchi (23.412N, 85.440E; India) utilized in the present study can be obtained from the Indian National Centre for Ocean Information Service upon request (<http://www.incois.gov.in/portal/datainfo/ctczdata.jsp>). Hourly ERA5-Land reanalysis data utilized in this study can be found in its official website <https://cds.climate.copernicus.eu/cdsapp#!/dataset/reanalysis-era5-land?tab=form>.

**Author contribution:** All authors contributed to the design of the study, analysis, and writing of the manuscript. PN carried out the computations as well as the analysis of the model output.

**Competing interests:** The authors have declared that they have no conflict of interest.

#### **Acknowledgements:**

We would like to thank Dr. Manoj Kumar for providing observational data at Ranchi. The authors acknowledge the use of NCAR-NCL and ERA5-Land reanalysis dataset for this study. The use of supercomputing facility (HPC) provided by IIT Delhi is gratefully acknowledged. This work is partially supported by INSA, DST, DST-INSPIRE, and YES Foundation. We wish to thank the reviewers for their helpful comments and suggestions, which have significantly enhanced the quality of this paper.

590 **References:**

- 591 Bruin, H. A. R. de.: A Note on Businger's Derivation of Nondimensional Wind and Temperature Profiles under Unstable  
592 Conditions, *J. Appl. Meteor. Climatol.*, 38, 626–28, [https://doi.org/10.1175/1520-0450\(1999\)038<0626:ANOBSD>2.0.CO;2](https://doi.org/10.1175/1520-0450(1999)038<0626:ANOBSD>2.0.CO;2),  
593 1999.
- 594 Brutsaert, W.: Stability Correction Functions for the Mean Wind Speed and Temperature in the Unstable Surface Layer,  
595 *Geophys. Res. Lett.*, 19, 469–72. <https://doi.org/10.1029/92GL00084>, 1992.
- 596 Businger, J. A., Wyngaard, J. C., Izumi, Y., & Bradley, E. F. 1971. "Flux-Profile Relationships in the Atmospheric Surface  
597 Layer in the Atmospheric Surface Layer". *J. Atmos. Sci.*, 28(2), 181-189. [https://doi.org/10.1175/1520-0469\(1971\)028<0181:FPRITA>2.0.CO;2](https://doi.org/10.1175/1520-0469(1971)028<0181:FPRITA>2.0.CO;2), 1971.
- 599 Carl, D. M., Tarbell, T. C., and Panofsky, H. A.: Profiles of Wind and Temperature from Towers over Homogeneous Terrain,  
600 *J. Atmos. Sci.*, 30, 788-794, [http://dx.doi.org/10.1175/1520-0469\(1973\)030<0788:POWATF>2.0.CO;2](http://dx.doi.org/10.1175/1520-0469(1973)030<0788:POWATF>2.0.CO;2), 1973.
- 601 Cheng, Y., and Brutsaert, W.: Flux-Profile Relationships for Wind Speed and Temperature in the Stable Atmospheric  
602 Boundary Layer, *Boundary-Layer Meteorol.*, 114, 519–38. <https://doi.org/10.1007/s10546-004-1425-4>, 2005.
- 603 Dwivedi, A. K., Chandra, S., Kumar, M., Kumar, S., and Kumar, N. V. P. K.: Spectral Analysis of Wind and Temperature  
604 Components during Lightning in Pre-Monsoon Season over Ranchi, *Meteorol. Atmos. Phys.*, 127, 95–105,  
605 <https://doi.org/10.1007/s00703-014-0346-0>, 2015.
- 606 Dyer, A. J.: A Review of Flux-Profile Relationships, *Boundary-Layer Meteorol.*, 7, 363–372.  
607 <https://doi.org/10.1007/BF00240838>, 1974.
- 608 Fairall, C. W., Bradley, E. F., Hare, J. E., Grachev, A. A., and Edson, J. B.: Bulk Parameterization of Air–Sea Fluxes: Updates  
609 and Verification for the COARE Algorithm, *J. Climate*, 16, 571–591, [https://doi.org/10.1175/1520-0442\(2003\)016<0571:BPOASF>2.0.CO;2](https://doi.org/10.1175/1520-0442(2003)016<0571:BPOASF>2.0.CO;2), 2003.
- 611 Fairall, C. W., Bradley, E. F., Rogers, D. P., Edson, J. B., and Young, G. S.: Bulk Parameterization of Air-Sea Fluxes for  
612 Tropical Ocean global Atmosphere Coupled-Ocean Atmosphere Response Experiment, *J. Geophys. Res.*, 101, 3747–3764,  
613 doi:[10.1029/95JC03205](https://doi.org/10.1029/95JC03205), 1996.
- 614 Friedl, M. A., McIver, D. K., Hodges, J. C. F., Zhang, X. Y., Muchoney, D., Strahler, A. H., Woodcock, C. E., Gopal, S.,  
615 Schneider, A., Cooper, A., Baccini, A., Gao, F., and Schaaf, C.: Global Land Cover Mapping from MODIS: Algorithms and  
616 Early Results, *Remote Sens. Environ.* 83, 287–302, [https://doi.org/10.1016/S0034-4257\(02\)00078-0](https://doi.org/10.1016/S0034-4257(02)00078-0), 2002.
- 617 Giorgi, F., Coppola, E., Solmon, F., Mariotti, L., Sylla, M. B., Bi, X., Elguindi, N., et al.: RegCM4: Model Description and  
618 Preliminary Tests over Multiple CORDEX Domains, *Clim. Res.*, 52, 7–29, <http://doi.org/10.3354/cr01018>, 2012.
- 619 Grachev, A. A., Fairall, C. W., and Bradley, E. F.: Convective Profile Constants Revisited, *Boundary-Layer Meteorol.*, 94,  
620 495–515, <https://doi.org/10.1023/A:1002452529672>, 2000.

621 Grachev, A. A., Andreas, E. L., Fairall, C. W., Guest, P. S., and Persson, P. O. G.: SHEBA Flux-Profile Relationships in the  
622 Stable Atmospheric Boundary Layer, *Boundary-Layer Meteorol.*, 124, 315–33, <https://doi.org/10.1007/s10546-007-9177-6>,  
623 2007.

624 Grell, G. A., Dudhia, J., & Stauffer, D.: A description of the fifth-generation Penn State/NCAR Mesoscale Model (MM5) (No.  
625 NCAR/TN-398+STR), University Corporation for Atmospheric Research. <http://doi:10.5065/D60Z716B>, 1994.

626 Hicks, B. B.: Wind Profile Relationships from the ‘Wangara’ Experiment, *Q. J. R. Meteorol. Soc.*, 102, 535–51,  
627 <https://doi.org/10.1002/qj.49710243304>, 1976.

628 Hogstrom, U.: Review of Some Basic Characteristics of the Atmospheric Surface Layer, *Boundary-Layer Meteorol.*, 78, 215–  
629 246, <https://doi.org/10.1007/BF00120937>, 1996.

630 Holtslag, A. A. M., and De Bruin, H. A. R.: Applied Modeling of the Night-time Surface Energy Balance over Land, *J. Appl.*  
631 *Meteor. Climatol.*, 27, 689–704. [https://doi.org/10.1175/1520-0450\(1988\)027<0689:AMOTNS>2.0.CO;2](https://doi.org/10.1175/1520-0450(1988)027<0689:AMOTNS>2.0.CO;2), 1988.

632 Jiménez, P. A., González-Rouco, J. F., García-Bustamante, E., Navarro, J., Montávez, J. P., de Arellano, J. V., Dudhia, J., &  
633 Muñoz-Roldan, A.: Surface Wind Regionalization over Complex Terrain: Evaluation and Analysis of a High-Resolution WRF  
634 Simulation, *J. Appl. Meteor. Climatol.*, 49, 268–287, <https://doi.org/10.1175/2009JAMC2175.1>, 2010.

635 Jiménez, P. A., Dudhia, J., González-Rouco, J. F., Navarro, J., Montávez, J. P., & García-Bustamante, E.: A Revised Scheme  
636 for the WRF Surface Layer Formulation, *Mon. Wea. Rev.*, 140, 898–918. <https://doi.org/10.1175/MWR-D-11-00056.1>, 2012.

637 Kader, B. A., and Yaglom, A. M.: Mean Fields and Fluctuation Moments in Unstably Stratified Turbulent Boundary Layers,  
638 *Journal of Fluid Mechanics*, 212, 637–662, <https://doi.org/10.1017/S0022112090002129>, 1990.

639 Monin, A. S., and Obukhov, A. M.: Basic Laws of Turbulent Mixing in the Surface Layer of the Atmosphere, *Tr. Akad. Nauk*  
640 *SSSR Geophys. Inst* 24(151), 163–187, 1954.

641 Namdev, P., Sharan, M. & Mishra, S.K.: Impact of the similarity functions of surface layer parametrization in a climate model  
642 over the Indian region, *Q. J. R. Meteorol. Soc.*, 149, 152–170, <https://doi.org/10.1002/qj.4400>, 2023.

643 Panofsky, H. and Dutton, J.: *Atmospheric Turbulence*, John Wiley & Sons, New York, 397 p, 1984.

644 Rao, K. G., Narasimha, R., and Prabhu, A.: Estimation of Drag Coefficient at Low Wind Speeds over the Monsoon Trough  
645 Land Region during MONTBLEX-90, *Geophys. Res. Lett.*, 23, 2617–2620, <https://doi.org/10.1029/96GL02368>, 1996.

646 Rao, K. G., and Narasimha, R.: Heat-Flux Scaling for Weakly Forced Turbulent Convection in the Atmosphere, *Journal of*  
647 *Fluid Mechanics*, 547, 115–135, <https://doi.org/10.1017/S0022112005007251>, 2006.

648 Sharan, M., and Srivastava, P.: Characteristics of the Heat Flux in the Unstable Atmospheric Surface Layer, *J. Atmos. Sci.*,  
649 73, 4519–4529, <https://doi.org/10.1175/JAS-D-15-0291.1>, 2016.

650 Srivastava, P., and Sharan, M.: Characteristics of the Drag Coefficient over a Tropical Environment in Convective Conditions,  
651 *J. Atmos. Sci.*, 72, 4903–4913, <https://doi.org/10.1175/JAS-D-14-0383.1>, 2015.

652 Srivastava, P., and Sharan, M.: Analysis of Dual Nature of Heat Flux Predicted by Monin-Obukhov Similarity Theory: An  
653 Impact of Empirical Forms of Stability Correction Functions, *J. Geophys. Res. Atmos.*, 124, 3627–3646,  
654 <https://doi.org/10.1029/2018JD029740>, 2019.

655 Srivastava, P., and Sharan, M.: Uncertainty in the Parameterization of Surface Fluxes under Unstable Conditions, *J. Atmos.*  
656 *Sci.*, 78, 2237–2247, <https://doi.org/10.1175/JAS-D-20-0350.1>, 2021.

657 Srivastava, P., Sharan, M., and Kumar, M.: A Note on Surface Layer Parameterizations in the Weather Research and Forecast  
658 Model, *Dynam. Atmos. Ocean*, 96, 101259, <https://doi.org/10.1016/j.dynatmoce.2021.101259>, 2021.

659 Srivastava, P., Sharan, M., Kumar, M., and Dhuria, A. K.: On Stability Correction Functions over the Indian Region under  
660 Stable Conditions, *Meteorol. Appl.*, 27:e1880, <https://doi.org/10.1002/met.1880>, 2020.

661 Stull, R. B.: *An Introduction to Boundary Layer Meteorology*, Kluwer Academic Publishers, Dordrecht, The Netherlands, 13,  
662 670 pp, <https://doi.org/10.1007/978-94-009-3027-8>, 1988.

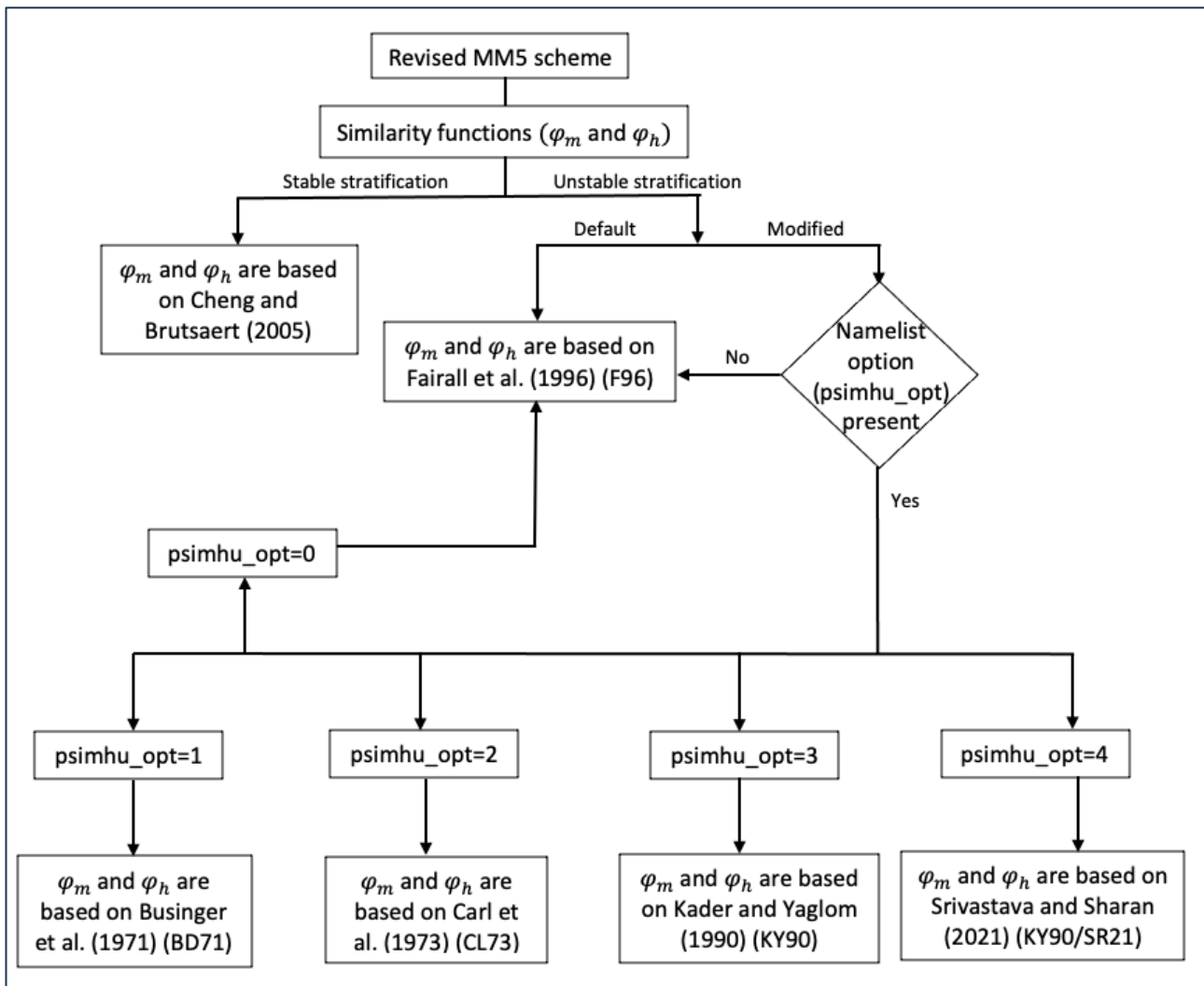
663 Venkatram, A.: Applying a framework for evaluating the performance of air quality models, in: *Proceedings of the sixth*  
664 *International Conference on Harmonisation within Atmospheric Dispersion modeling for Regulatory Applications*, Rouen,  
665 France, 11 – 14 October, 1999, 11 – 14, 1999.

666 Webb, E. K.: Profile Relationships: The Log-linear Range, and Extension to Strong Stability, *Q. J. R. Meteorol. Soc.*, 96, 67–  
667 90, <https://doi.org/10.1002/qj.49709640708>, 1970.

668 Wilson, D. K.: An Alternative Function for the Wind and Temperature Gradients in Unstable Surface Layers, *Boundary-Layer*  
669 *Meteorol.*, 99, 151–158, <https://doi.org/10.1023/A:1018718707419>, 2001.

670 Zeng, X., Zhao, M., and Dickinson, R. E.: Intercomparison of Bulk Aerodynamic Algorithms for the Computation of Sea  
671 Surface Fluxes Using TOGA COARE and TAO Data, *J. Climate*, 11, 2628–2644, [https://doi.org/10.1175/1520-0442\(1998\)011<2628:IOBAAF>2.0.CO;2](https://doi.org/10.1175/1520-0442(1998)011<2628:IOBAAF>2.0.CO;2), 1998.

673

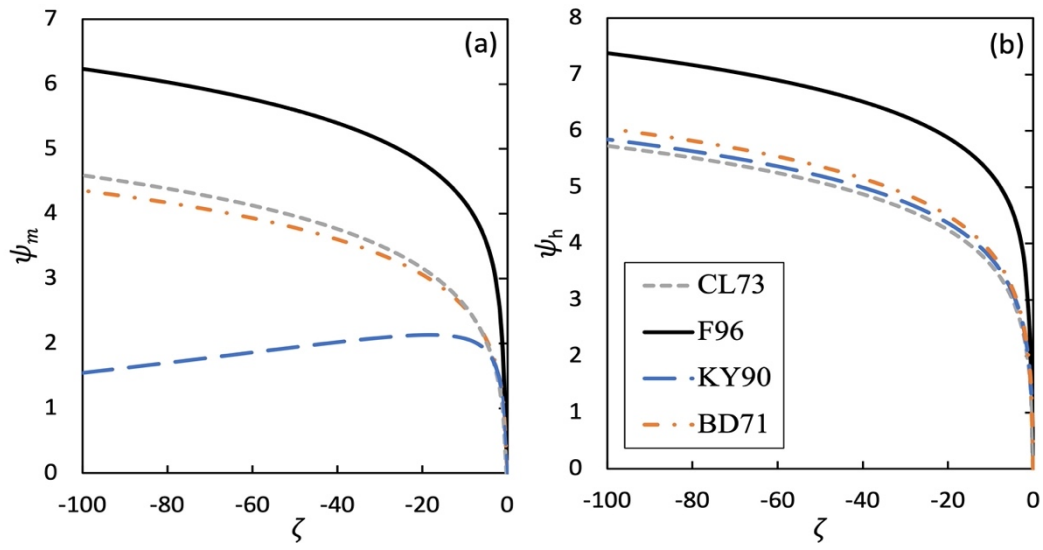


674

675 **Figure 1: Flowchart to provide a brief description of different options for similarity functions in the modified surface layer scheme**  
 676 **that can be controlled by namelist variable psimhu\_opt.**

677





679 **Figure 2:** Integrated similarity functions  $\psi_{m,h}(\zeta)$  for momentum and heat for default (F96; black line) and newly installed (BD71,  
 680 CL73, and KY90; orange, grey and blue lines, respectively) functions for unstable atmospheric surface layer.

681

682

683

684

685

686

687

688

689

690

691

692

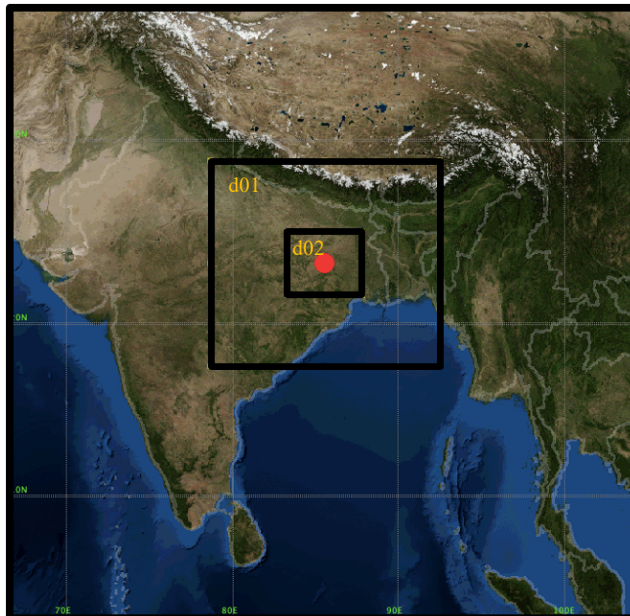
693

694

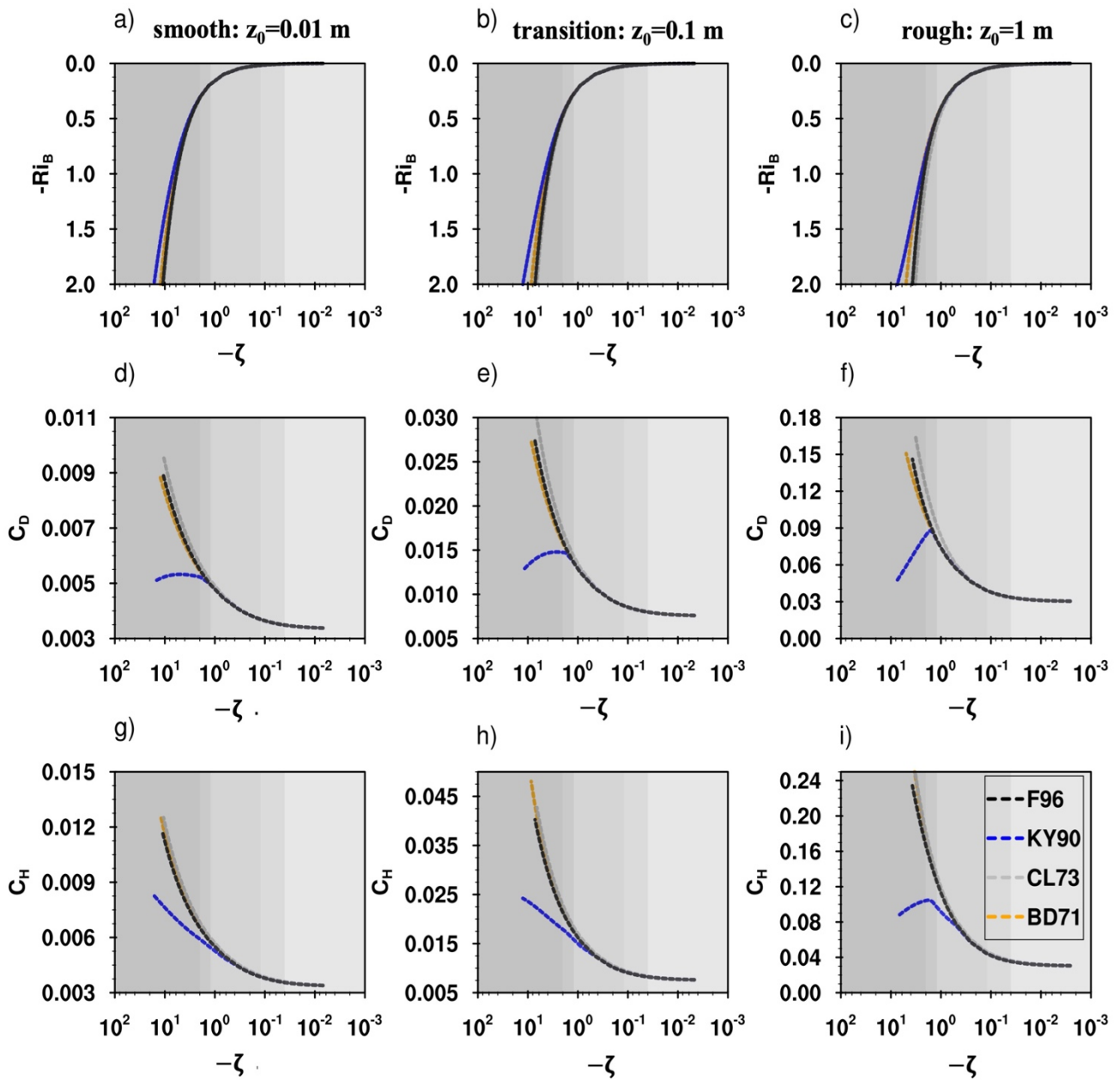
695

696

697



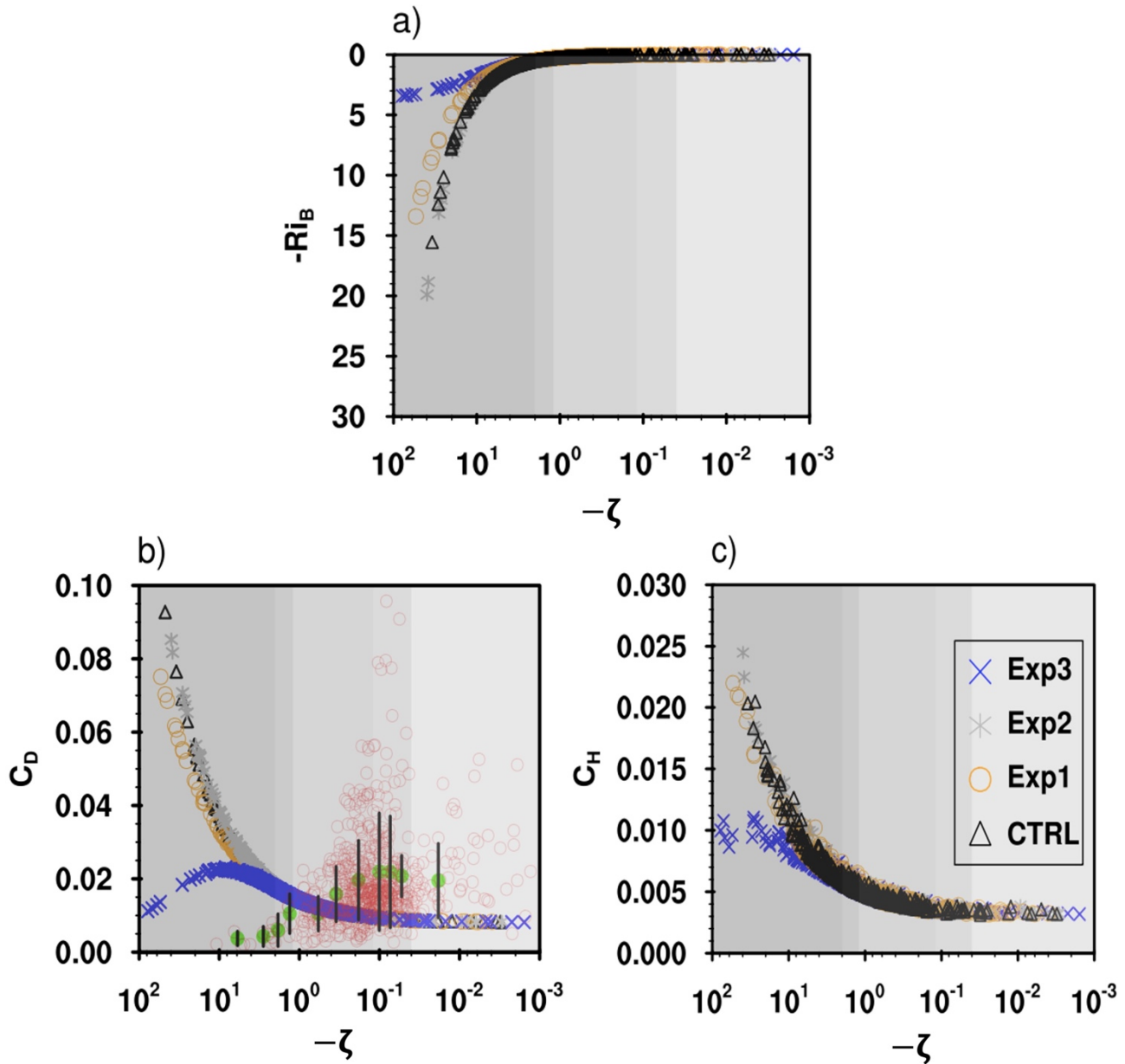
698 **Figure 3:** Spatial distribution of domain used for the simulations using the WRF model. The spatial resolution for domains d01 and  
 699 d02 is  $6 \times 6$  km and  $2 \times 2$  km, respectively. The domain d02 covers  $446 \times 392$  km<sup>2</sup> area around the centre point.



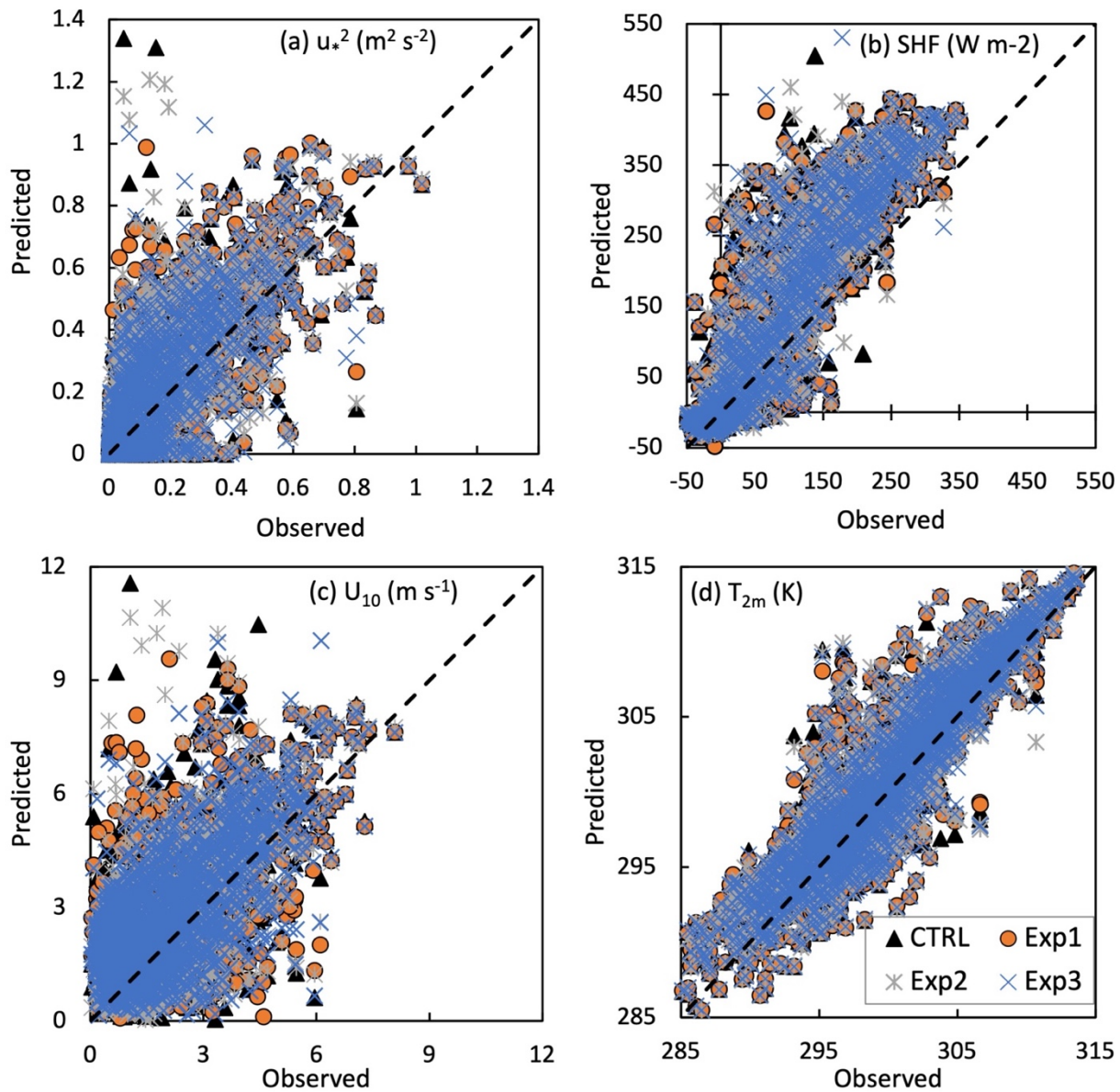
701

702 **Figure 4: Variation of  $\zeta$  with  $Ri_B$  (upper panel),  $C_D$  (middle panel) and  $C_H$  (lower panel) with  $\zeta$  calculated from bulk flux algorithm**  
 703 **(offline simulation) for different functional forms of  $\psi_m$  and  $\psi_h$  corresponding to BD71, CL73, KY90, and F96 forms for smooth**  
 704 **( $z_0 = 0.01$  m; 1<sup>st</sup> column), transition ( $z_0 = 0.1$  m; 2<sup>nd</sup> column), and rough ( $z_0 = 1.0$  m; 3<sup>rd</sup> column) surfaces. The background**  
 705 **colour corresponds to different sublayers in convective conditions (Kader and Yaglom 1990), from the dynamic sublayer ( $0 \geq \zeta >$**   
 706  **$-0.04$ ; light grey) to the free convective sublayer ( $\zeta < -2$ ; dark grey).**

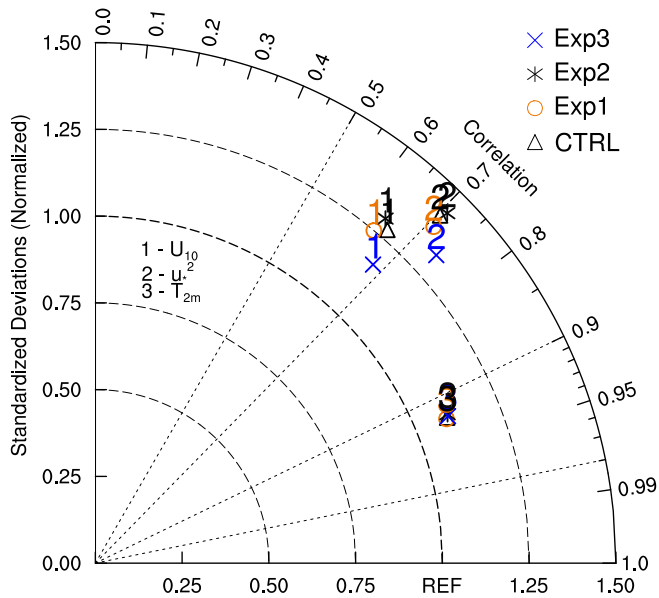
707



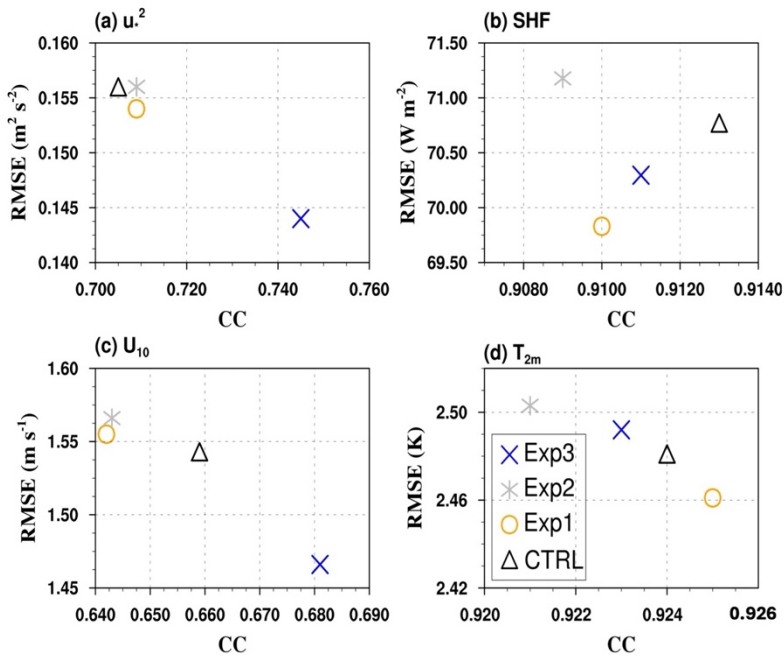
711 Figure 5: Variation of model simulated (a)  $\zeta$  with  $\text{Ri}_B$ , (b)  $C_D$  and (c)  $C_H$  with  $\zeta$  from different experiments using different  $\psi_m$  and  
 712  $\psi_h$  corresponding to F96 (CTRL), BD71 (Exp1), CL73 (Exp2), and KY90 (Exp3) under convective conditions. The red circles in (b)  
 713 denote the observed  $C_D$  with  $\zeta$  at the location of flux tower. The mean values of observed  $C_D$  in each sublayer are shown with green  
 714 solid circles along with standard deviations in the form of error bars. Depending upon the data availability, two or three bins of  
 715 equal width are chosen in each sublayer. The background colour corresponds to different sublayers in convective conditions (Kader  
 716 and Yaglom 1990), from the dynamic sublayer ( $0 \geq \zeta > -0.04$ ; light grey) to the free convective sublayer ( $\zeta < -2$ ; dark grey).



718 Figure 6: Scatter plot of model simulated (a)  $u_*^2$  ( $\text{m}^2 \text{s}^{-2}$ ) (representative of momentum flux), (b) SHF ( $\text{W m}^{-2}$ ) (sensible heat flux), (c)  
 719  $U_{10}$  ( $\text{m s}^{-1}$ ) (wind speed at 10 m height), and (d)  $T_{2m}$  (K) (temperature at 2 m height) vs observed values at the location of flux tower  
 720 at Ranchi (23.412oN, 85.440oE), India (centre point of the domain) during pre-monsoon season (MAM).

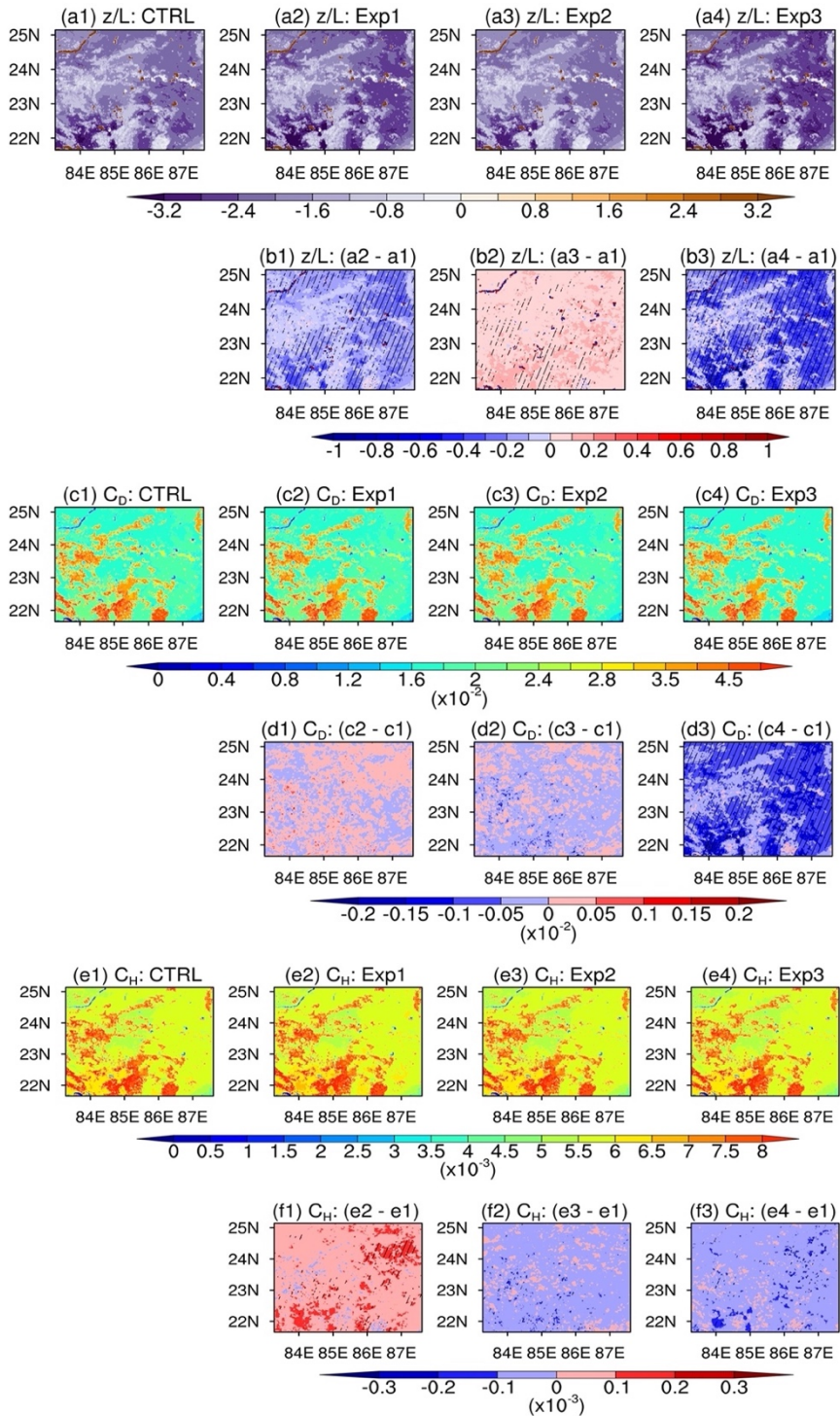


723 **Figure 7: Taylor diagram showing the correlation coefficient, normalized standard deviations for  $U_{10}$ ,  $u_*^2$ , and  $T_{2m}$  from different**  
 724 **experiments together with CTRL simulation with respect to observations derived from flux tower installed at Ranchi (23.412°N,**  
 725 **85.440°E), India.**

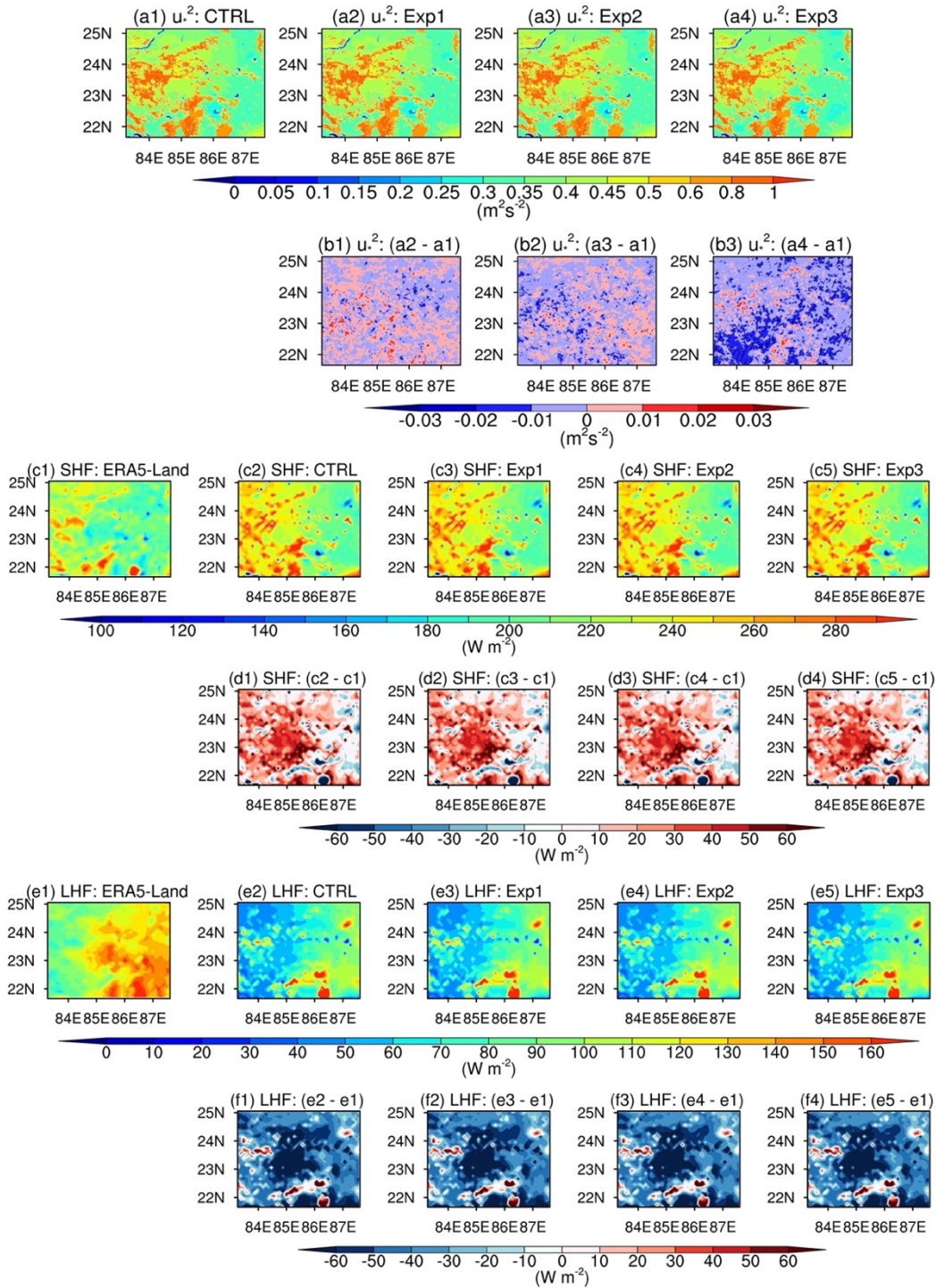


726 **Figure 8: Scatter plot between correlation coefficient (CC) and root mean square error (RMSE) for (a)  $u_*^2$ , (b) SHF, (c)  $U_{10}$ , and (d)**  
 727  **$T_{2m}$  simulated by various experiments (Exp1-3) together with CTRL simulation for pre-monsoon season (MAM; 2009) at the location**  
 728 **of the flux tower (23.412°N, 85.440°E).**





729 **Figure 9: Mean spatial distribution of model simulated  $\zeta$  (1<sup>st</sup> row),  $C_D$  (3<sup>rd</sup> row) and  $C_H$  (5<sup>th</sup> row) from different experiments and**  
 730 **their differences with respect to CTRL simulation averaged during daytime for whole simulation period. Hatched regions show**  
 731 **significant differences at 95% confidence level in experiments with respect to CTRL simulation.**



732 Figure 10: Mean spatial distribution of simulated  $u_*^2$  (1<sup>st</sup> row) from different experiments and their differences (2<sup>nd</sup> row) with respect  
733 to CTRL simulation. SHF and LHF from ERA5-Land reanalysis and simulated using various experiments and their differences  
734 with respect to ERA5-Land data averaged during daytime for the whole simulation period are shown. Hatched regions show  
735 significant differences at 95% confidence level in experiments with respect to CTRL simulation.



736

737

738

739

740

741

742

743

744

745

746

747

748

749

750

751

752

753

754

755

756

757

758

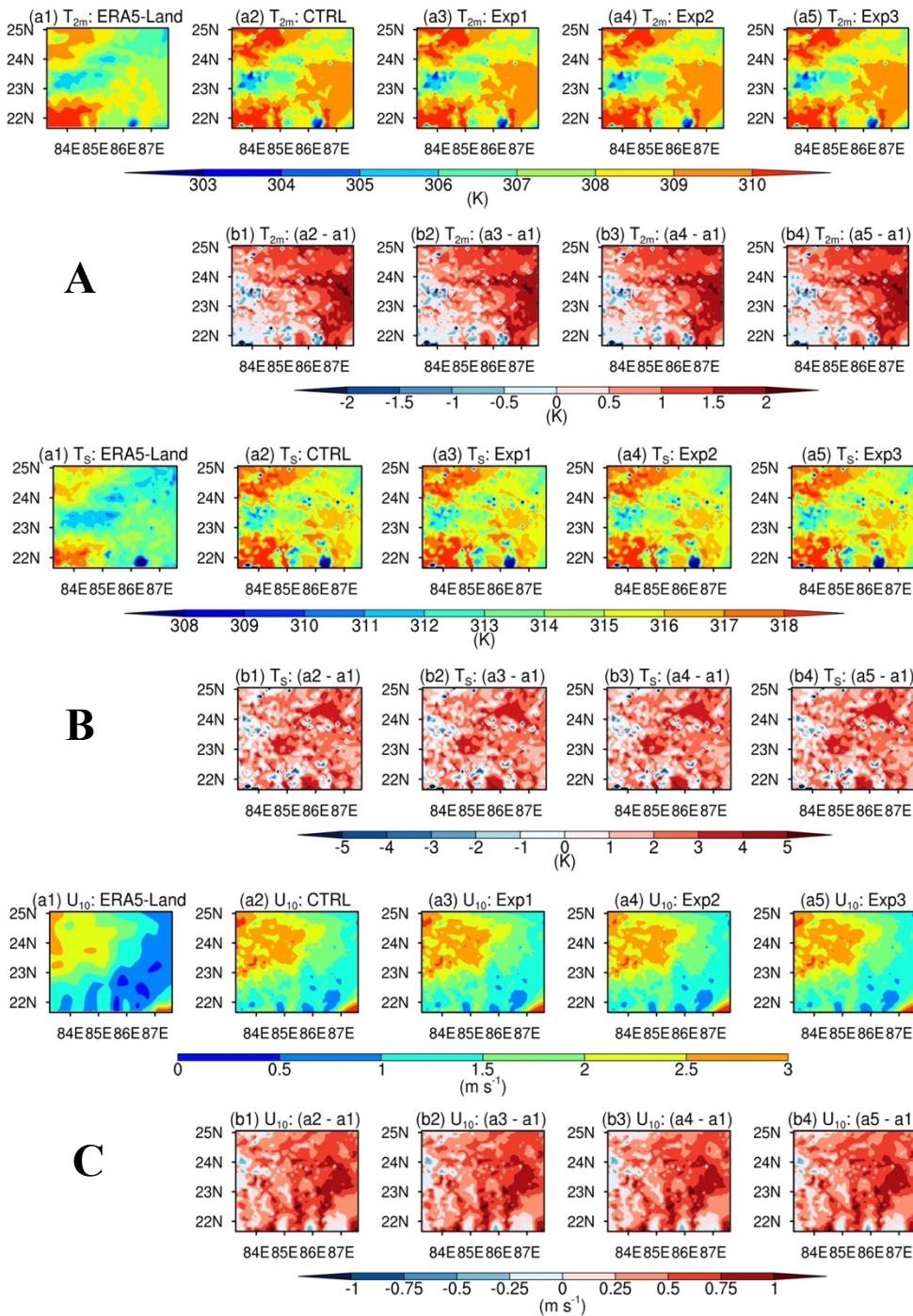
759

760

761

762

763



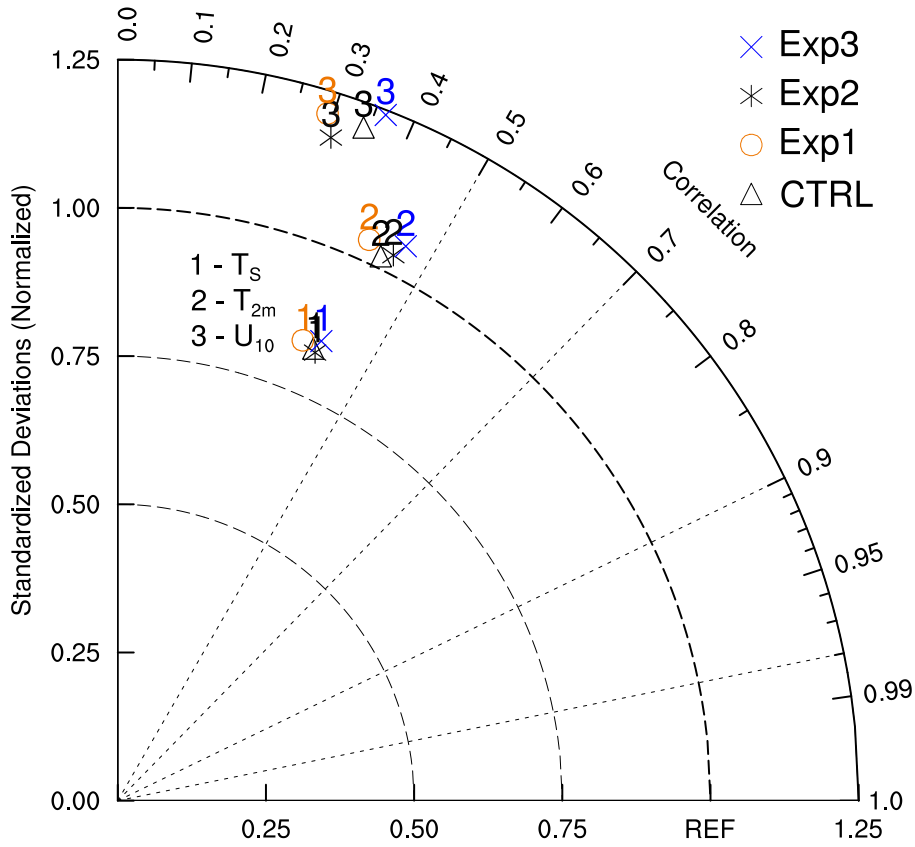
764

765

766

Figure 11: In upper panel (A), mean spatial distribution of  $T_{2m}$  from ERA5-Land reanalysis (a1) and simulated using different experiments (a2-a5) and their differences with respect to ERA5-Land reanalysis (b1-b4) averaged during daytime for the whole simulation period. Middle (Lower) panel is same as the upper panel but for  $T_S$  ( $U_{10}$ ).





768 **Figure 12: Taylor diagram showing the correlation coefficient, normalized standard deviations for  $T_s$  (K),  $T_{2m}$  (K), and  $U_{10}$  ( $m\ s^{-1}$ )**  
 769 **from different experiments together with CTRL simulation with respect to ERA5-Land reanalysis dataset averaged during strong**  
 770 **convective conditions (hours during daytime in which  $\zeta$  is smaller than  $-10$ ) for whole simulation period.**

771

772

773

774

775

776

777

778

779

780

781

782 **Table 1. Description of various simulations conducted in this study.**

<b>Experiments</b>	<b>Description</b>
CTRL	Simulation using default surface layer scheme with F96 functions
Exp1	Simulation using surface layer scheme with BD71 functions
Exp2	Simulation using surface layer scheme with CL73 functions
Exp3	Simulation using surface layer scheme with newly installed KY90 functions

783

784

785

786

787

788

789

790

791

792

793

794

795

796

797

798

799

800

801

802

803

804 Table 2: Comparison statistics for  $u_*^2$  ( $\text{m}^2 \text{s}^{-2}$ ), SHF ( $\text{W m}^{-2}$ ),  $U_{10}$  ( $\text{m s}^{-1}$ ), and  $T_{2m}$  (K) simulated using different experiments together  
805 with CTRL simulation with respect to observations derived from flux tower at Ranchi (India) for MAM season. The mean absolute  
806 error (MAE), root mean square error (RMSE), mean bias (MB), index of agreement (IOA), and correlation coefficient (CC) are  
807 shown.

MAM		$u_*^2$ ( $\text{m}^2 \text{s}^{-2}$ )	SHF ( $\text{W m}^{-2}$ )	$U_{10}$ ( $\text{m s}^{-1}$ )	$T_{2m}$ (K)
CTRL	MAE	0.09	43.46	1.20	1.82
	RMSE	0.16	70.77	1.54	2.48
	MB	0.03	34.88	0.83	0.93
	IOA	0.82	0.89	0.73	0.95
	CC	0.71	0.91	0.66	0.92
Exp1	MAE	0.09	<b>42.72</b>	1.20	<b>1.81</b>
	RMSE	0.15	<b>69.83</b>	1.56	<b>2.46</b>
	MB	0.03	<b>33.06</b>	0.81	0.90
	IOA	0.82	0.89	0.72	<b>0.96</b>
	CC	0.71	0.91	0.64	<b>0.93</b>
Exp2	MAE	0.09	43.55	1.20	1.84
	RMSE	0.16	71.18	1.57	2.50
	MB	0.03	34.49	0.81	<b>0.87</b>
	IOA	0.82	0.89	0.72	0.95
	CC	0.71	0.91	0.64	0.92
Exp3	MAE	<b>0.08</b>	42.96	<b>1.16</b>	1.83
	RMSE	<b>0.14</b>	70.30	<b>1.47</b>	2.49
	MB	<b>0.03</b>	33.47	<b>0.78</b>	0.91
	IOA	<b>0.84</b>	0.89	<b>0.75</b>	0.95
	CC	<b>0.74</b>	0.91	<b>0.68</b>	0.92

808

809

810

811

812

813

814

815

816

817

818 Table 3: Comparison statistics for  $T_{2m}$  (K),  $T_s$  (K), and  $U_{10}$  ( $m s^{-1}$ ) simulated using different experiments together with CTRL  
 819 simulation with respect to ERA5-Land reanalysis data averaged during strong unstable stratification (hours during daytime in  
 820 which  $\zeta$  is smaller than  $-10$ ) for whole simulation period. The percent mean bias (Bias %), pattern correlation coefficient (PCC),  
 821 and root mean square error (RMSE) are shown.

MAM	$T_s$ (K)			$T_{2m}$ (K)			$U_{10}$ ( $m s^{-1}$ )		
	Bias (%)	RMSE	PCC	Bias (%)	RMSE	PCC	Bias (%)	RMSE	PCC
CTRL	1.26	4.01	0.40	0.64	2.13	0.43	-4.96	0.44	0.34
Exp1	1.26	4.03	0.37	0.64	2.16	0.40	-4.43	0.45	0.29
Exp2	1.25	3.99	0.40	0.63	2.10	0.45	-5.39	0.44	0.31
Exp3	<b>1.24</b>	<b>3.97</b>	<b>0.41</b>	<b>0.62</b>	<b>2.10</b>	<b>0.46</b>	<b>-0.28</b>	0.47	<b>0.36</b>

822

823

824